

Apparatus for measurement of the electric dipole moment of the neutron using a cohabiting atomic-mercury magnetometer

Article (Submitted Version)

Baker, C A, Chibane, Y, Chouder, M, Geltenbort, P, Green, K, Harris, P G, Heckel, B R, Ilaydjiev, P, Ivanov, S N, Kilvington, I, Lamoreaux, S K, May, D J, Pendlebury, J M, Richardson, J D, Shiers, D B et al. (2014) Apparatus for measurement of the electric dipole moment of the neutron using a cohabiting atomic-mercury magnetometer. Nuclear Instruments and Methods in Physics Research Section A: Accelerators, Spectrometers, Detectors and Associated Equipment, 736. pp. 184-203. ISSN 0168-9002

This version is available from Sussex Research Online: <http://sro.sussex.ac.uk/id/eprint/45253/>

This document is made available in accordance with publisher policies and may differ from the published version or from the version of record. If you wish to cite this item you are advised to consult the publisher's version. Please see the URL above for details on accessing the published version.

Copyright and reuse:

Sussex Research Online is a digital repository of the research output of the University.

Copyright and all moral rights to the version of the paper presented here belong to the individual author(s) and/or other copyright owners. To the extent reasonable and practicable, the material made available in SRO has been checked for eligibility before being made available.

Copies of full text items generally can be reproduced, displayed or performed and given to third parties in any format or medium for personal research or study, educational, or not-for-profit purposes without prior permission or charge, provided that the authors, title and full bibliographic details are credited, a hyperlink and/or URL is given for the original metadata page and the content is not changed in any way.

Apparatus for Measurement of the Electric Dipole Moment of the Neutron using a Cohabiting Atomic-Mercury Magnetometer

C.A. Baker^a, Y. Chibane^b, M. Chouder^b, P. Geltenbort^c, K. Green^a, P.G.
Harris^{b,*}, B.R. Heckel^d, P. Iaydjiev^{a,1}, S.N. Ivanov^{a,3}, I. Kilvington^a, S.K.
Lamoreaux^{d,4}, D.J. May^b, J.M. Pendlebury^b, J.D. Richardson^b, D.B. Shiers^b,
K.F. Smith^{b,5}, M. van der Grinten^a

^aRutherford Appleton Laboratory, Chilton, Didcot, Oxon OX11 0QX, UK

^bUniversity of Sussex, Falmer, Brighton BN1 9QH, UK

^cInstitut Laue-Langevin, BP 156, F-38042 Grenoble Cedex 9, France

^dDepartment of Physics, University of Washington, Seattle, WA 98195

Abstract

A description is presented of apparatus used to carry out an experimental search for an electric dipole moment of the neutron, at the Institut Laue-Langevin (ILL), Grenoble. The experiment incorporated a cohabiting atomic-mercury magnetometer in order to reduce spurious signals from magnetic field fluctuations. The result has been published in an earlier letter [1]; here, the methods and equipment used are discussed in detail.

Keywords: neutron, EDM, mercury magnetometer

1. Introduction

1.1. The electric dipole moment of the neutron

Any non-degenerate system of defined, non-zero angular momentum will have a permanent electric dipole moment (EDM) d if its interactions are asymmetric under both parity (P) and time (T) inversion [2–4]. The neutron carries

*Corresponding author

¹On leave of absence from INRNE, Sofia, Bulgaria

²On leave of absence from Petersburg Nuclear Physics Institute, Russia

³Present address: Institut Laue-Langevin, BP 156, F-38042 Grenoble Cedex 9, France

⁴Present address: Department of Physics, Yale University, New Haven, CT 06520

⁵Deceased

spin $\frac{1}{2}$, and it also possesses the virtue of being sensitive to all known particle physics interactions. It is therefore expected to possess a finite EDM with its magnitude dependent upon the nature and origin of the T violation, and this EDM is, in turn, a sensitive probe of such asymmetric interactions.

Parity violation [5] is a well-established property of the weak interaction in general. Evidence for T violation, which arises at a much weaker level, has come from the observation that there is a (0.66 ± 0.18) % greater probability for a \bar{K}^0 to turn into a K^0 than the other way around [6], and that there is an angular asymmetry in the rare decay $K_L \rightarrow \pi^+ \pi^- e^+ e^-$ of $(14.6 \pm 2.3 \pm 1.1)$ % [7, 8]. T violation and CP violation, where C is charge conjugation, are closely related through the CPT theorem [9–11] which predicts the invariance of the combined symmetry. Any CP violation in a CPT-invariant theory therefore implies the breakdown of time-reversal symmetry and leaves a finite expectation value of the neutron EDM. Violation of CP-symmetry has been studied in detail in the K^0 system [12] and, more recently, in the B system [13, 14]; see, for example, [15] and references therein.

The origins of CP violation are still unknown. In the kaon system it is dominated by indirect ($\Delta S = 2$) contributions due to mixing. It has been observed [16, 17] in direct quark interactions ($\Delta S = 1$). Contributions from “superweak” $\Delta S = 2$ interactions specific to the kaon systems have been ruled out.

Many alternative theories exist (see, for example, contributions in [18]), but the data from the K^0 and b systems alone are insufficient to distinguish between them. These theories also predict non-zero values for the EDM of the neutron, but the predictions differ, one from another, by many orders of magnitude [19]. The major difference between the theories is that in some, and in particular in the standard $SU(2) \times U(1)$ model of electroweak interactions, the contributions to the EDM appear only in second order in the weak interaction coupling coefficient, whereas in others the contributions are of first order in the weak interaction. Detection of the latter larger size of EDM would be evidence for new physics beyond the standard model [20]. The small size of the neutron EDM,

as indicated by the measured values displayed in Fig. 1 [1, 21–37], has already eliminated many theories, and is pressing heavily upon the expectations from extensions to the Standard Model through to supersymmetric interactions.

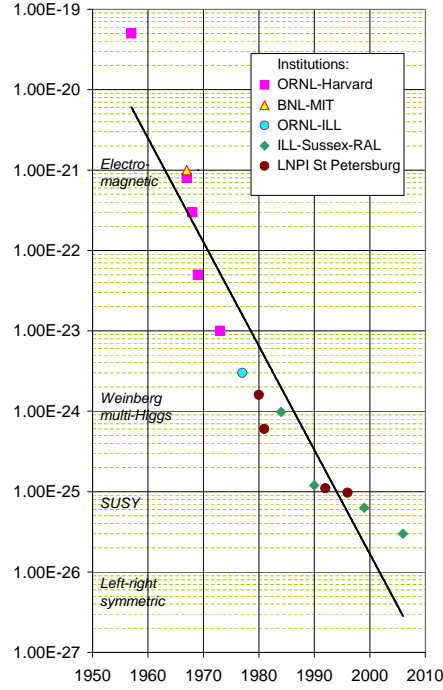


Figure 1: The evolution of the experimental limit of the electric dipole moment of the neutron. Those experiments before 1980 used neutron beams, and those after use stored ultracold neutrons. See [19] for the theoretical predictions.

1.2. Implications of non-zero EDM measurements

EDMs are being sought in various systems: the free neutron, the mercury atom [38], and the electron (via the thallium atom [39] and, more recently, the YbF [40], ThO [41] and PbO molecules [42, 43]), in addition to a proposal to study deuterium [44]. The fundamental mechanisms underlying sources of EDMs are different in each system, and the measurement of a finite value within one of these systems would therefore have distinctive implications [45]: For

example, if the EDMs are driven by the QCD θ angle, one would expect similar contributions to all strongly coupled systems, in which case the neutron, ^{199}Hg nucleus and the deuteron would all have EDMs of similar scale, whereas the electron EDM would be much smaller. Thus, the different systems have different implications for physics models beyond the standard model. Measurements on multiple systems are also needed in order to rule out cancellations.

EDM limits provide fairly tight constraints upon supersymmetric models; the same is true of most other models beyond the standard model that attempt to incorporate CP violation to a degree adequate to explain the observed baryon asymmetry of the Universe. The “accidental” cancellation of first-order contributions in the Standard Model is not a general feature, and EDM limits (and EDM values, once measured) provide a powerful way to distinguish between models and, indeed, to eliminate many of them. Ramsey [46] and Barr [17] have provided useful reviews of the situation, and the book by Khriplovich and Lamoreaux [47] contains further general information on EDMs.

2. Principle of the method

Almost all of the experimental searches for the EDM of the neutron have been magnetic resonance experiments in which polarized neutrons are subjected to parallel magnetic and electric fields in vacuum [48],[49]. The only internal degrees of freedom of the neutron are those associated with the spin \mathbf{s} , so that the Hamiltonian (\mathcal{H}) in an electric (\mathbf{E}_0) and a magnetic (\mathbf{B}_0) field is

$$\mathcal{H} = -2\mathbf{s} \cdot (\mu_n \mathbf{B}_0 + d_n \mathbf{E}_0). \quad (1)$$

If the magnetic and electric fields are parallel or antiparallel, the precession frequency ν_0 of the spin is given by

$$h\nu_0 = -2\mu_n |\mathbf{B}_0| \mp 2d_n |\mathbf{E}_0|, \quad (2)$$

where h is Planck’s constant, μ_n is the magnetic dipole moment ($-1.913\dots$ nuclear magnetons), d_n is the EDM and the upper (lower) sign is for \mathbf{B}_0 and \mathbf{E}

parallel (antiparallel). When an electric field of magnitude E_0 is changed from being parallel to \mathbf{B}_0 to being antiparallel, the precession frequency changes by

$$\delta\nu_0 = -\frac{4d_n E_0}{h}. \quad (3)$$

63 An EDM of 10^{-25} e cm would give a frequency shift of 1 μ Hz with the reversal of
 64 a 1 MV/m electric field. Because μ_n is negative, the sign definition for d_n is such
 65 that a positive dipole moment would increase the precession frequency when \mathbf{E}
 66 and \mathbf{B}_0 are antiparallel. Application of a magnetic field produces a magnetic
 67 Zeeman splitting; subsequent application of an electric field then merely changes
 68 the separation of the Zeeman levels, without inducing any further splitting. It
 69 should be noted that the electric polarizability of the neutron cannot affect the
 70 precession frequency to first order.

The early experiments used beams of neutrons with velocities greater than 100 m/s. Such experiments became limited by the $\mathbf{v} \times \mathbf{E}$ effect, according to which motion through the electric field results in a magnetic field in the neutron rest frame and hence a possible change in the precession frequency with the same dependence on the electric field as a real EDM. More recent experiments use ultra-cold neutrons (UCN), with velocities of less than 7 m/s, stored in evacuated chambers with walls that totally reflect the neutrons; the average velocity is so close to zero that the $\mathbf{v} \times \mathbf{E}$ effect can be adequately controlled at the present level of sensitivity. The first published result from a series of experiments being carried out under these conditions at the Institut Laue-Langevin (ILL) in Grenoble was $d_n = -(3 \pm 5) \times 10^{-26}$ e cm [34]. A broadly similar experiment at the PNPI in Russia [36] yielded an EDM of $(+2.6 \pm 4.0 \pm 1.6) \times 10^{-26}$ e cm. Both experiments were limited at the time by systematic uncertainties associated with instabilities and non-uniformities in the magnetic field. The ILL experiment initially used three rubidium magnetometers adjacent to the storage cell to try to compensate for magnetic field drifts; the PNPI experiment used instead a back-to-back twin-cell arrangement to make simultaneous measurements with the \mathbf{E} field in opposite directions. In each case, the presence of gradients in the magnetic field could adversely affect the results, since there

was a significant displacement between each measurement cell and the control volume used for compensation. This problem was addressed in this experiment at the ILL by the installation of a magnetometer based upon measurement of the precession frequency of spin-polarized $I = 1/2$ atoms of ^{199}Hg (3×10^{10} atoms/cm³; $\mu_n/\mu_{Hg} = \gamma_n/\gamma_{Hg} = -3.842$) stored simultaneously in the same trap as the neutrons. Using Eq. (2) for both the neutrons and the mercury, and assuming that both experience the same B , we find that to first order in the EDMs d ,

$$\frac{\nu_n}{\nu_{Hg}} = \left| \frac{\gamma_n}{\gamma_{Hg}} \right| + \frac{(d_n + |\gamma_n/\gamma_{Hg}| d_{Hg})}{\nu_{Hg}} E = \left| \frac{\gamma_n}{\gamma_{Hg}} \right| + \frac{d_{meas}}{\nu_{Hg}} E. \quad (4)$$

It is worth noting that Eq. (4) is only valid in a non-rotating reference frame. The rotation of the Earth imparts a small but perceptible shift in this frequency ratio [50].

For each data-taking run, the measured EDM d_{meas} was obtained from a linear fit to the ratio ν_n/ν_{Hg} versus E . Eq. (4) shows that d_{meas} contains in principle a contribution from d_{Hg} . The true d_{Hg} has however been shown to be $(0.49 \pm 1.29_{\text{stat}} \pm 0.76_{\text{syst}}) \times 10^{29}$ e cm, [38] so the systematic error thereby introduced into d_{meas} is a negligibly small $(-2 \pm 6) \times 10^{-29}$ e cm.

To the true d_n and d_{Hg} within d_{meas} there will also be added coefficients of fractional shifts in ν_n and ν_{Hg} , from other causes, which are linear in E and thus constitute additional systematic errors. The most important of these involves a geometric phase (GP) arising when the trapped particles experience a gradient $\partial B_{0z}/\partial z$ in the presence of E [51]. This particular effect has now been characterised and understood, and to a large extent it has been possible to compensate for it.

3. Ultracold neutrons

As a consequence of the coherent strong interaction between neutrons and the nuclei of a material medium, the surface of the medium presents a potential step relative to vacuum for long-wavelength neutrons. This potential V_F , called

the mean Fermi potential, is given by [52]

$$V_F = \frac{2\pi\hbar^2}{m}Nb, \quad (5)$$

where m is the mass of the neutron and N the number of atoms per unit volume with mean coherent forward scattering length b . A neutron with velocity less than the critical velocity v_c , defined by $mv_c^2/2 = V_F$, will be reflected from the surface for any angle of incidence. The Fermi potential for most materials is less than 300 neV, which corresponds to critical velocities of less than 7.6 m/s. Such slow neutrons can be confined in material traps by total external reflection, and are called ultra-cold neutrons (UCN). Nuclear reactors are a source of UCN, which constitute the very low energy part of the spectrum of moderated neutrons.

For cold and ultra-cold neutrons in a magnetic material the Fermi potential due to the nuclear scattering acquires an additional term representing the interaction of the magnetic moment of the neutron μ_n with the internal magnetic field B of the material. Thus,

$$V_F = \frac{2\pi\hbar^2}{m}Nb \pm \mu_n B, \quad (6)$$

where the \pm refers to the two spin states of the neutron. It is possible to find ferromagnetic materials with very low Fermi potentials for one spin state of the neutron and high Fermi potentials for the other spin state. It is then possible to spin-polarize UCN by transmission through a thin magnetised foil of such a material.

In the experiment described in this paper the number density of UCN was less than 10 cm^{-3} , and hence neutron-neutron collisions were extremely unlikely and can be ignored.

3.1. Upscattering and absorption of UCN in materials

Although the UCN have speeds characteristic of a temperature of about 2 mK, the neutron storage trap was maintained at room temperature. At first sight it might appear surprising that these neutrons could be stored for hundreds

of seconds without being scattered out of the UCN energy range. This was possible because the thermal motions of individual nuclei in the walls of the trap were sensed only weakly by the UCN, which were reflected by the combined coherent scattering from millions of nuclei lying within a short distance (of the order of 100 Å) of the surface. In this coherent scattering, the thermal motion of the center of mass of such a large group was negligible compared with the speed of the UCN. At the same time, any recoil energy associated with the group was also negligible. In addition, collisions that involved an exchange of energy with a smaller group of nuclei in the wall, and hence an upscattering of the neutron out of the UCN energy range, were infrequent (although important in determining the mean storage lifetime): the following argument has been given by Zeldovich [53]. When a neutron is reflected from a surface, its wave function penetrates into the wall a distance of order $(\lambda/2\pi)$, where λ is the de Broglie wavelength. In a storage volume of dimension l , each neutron with velocity v which is stored for a time T_s accumulates a total path length L inside the material of the walls, where

$$L \approx \frac{\lambda T_s v}{2\pi l}. \quad (7)$$

105 For the typical values of $T_s = 150$ s, speeds v of up to about 5 m/s, and
 106 $l = 150$ mm, a value of $L = 60$ μm is obtained. This distance is sufficiently
 107 small, compared with observed UCN interaction lengths, that one expects very
 108 little inelastic scattering and absorption of the neutrons.

109 In general, the survival times of UCN in material traps, particularly those
 110 made from materials with low absorption cross sections, are less than would
 111 be calculated for pure materials. This is caused by the presence of impurities
 112 (particularly hydrogen) in the surface, which drastically reduces the survival
 113 time [54, 55]. To reduce hydrocarbon contamination of the trap used in this
 114 EDM experiment, the majority of pumps in the vacuum system were oil-free
 115 turbopumps; the remaining diffusion pumps were filled with Fomblin [56] oil,
 116 which is a fully fluorinated polyether [57]. The chemical formula of Fomblin
 117 is $\text{CF}_3(\text{OCF}_3\text{CFCF}_2)_m(\text{OCF}_2)_n\text{OCF}_3$. To reduce the presence of surface hy-

drogen still further, the trap surfaces were discharge-cleaned using 1 torr of oxygen.

3.2. Depolarization in wall collisions

If neutrons are stored in a trap made of a material with non-zero magnetic moments, the interaction between a neutron and the wall will be spin dependent. Collisions with the walls will therefore result in depolarization of the neutrons. The magnitude of this depolarization can be estimated using a simple random walk model, similar to that of Goldenberg, Kleppner and Ramsey [58]. If, during one collision with the wall, the two spin states of the neutron experience Fermi potentials that differ by ΔV_F , and the interaction lasts a time τ , the spin of a neutron will be rotated through an angle

$$\delta\phi \approx \frac{\tau\Delta V_F}{\hbar}. \quad (8)$$

For the case where the neutron penetrates a distance $\lambda/2\pi$ into the wall,

$$\tau = \frac{\lambda}{2\pi v} \approx 2 \times 10^{-9} \text{ s}. \quad (9)$$

During the storage time the neutron makes $M = T_s v/l$ collisions with the walls, for which the phase shifts, which differ randomly from one wall collision to another, will add as in a random walk, so that the overall rms phase shift is

$$\Delta\phi \approx \overline{\delta\phi} \sqrt{M} = \frac{\overline{\Delta V_F} \lambda}{\hbar} \sqrt{\frac{T_s}{lv}}. \quad (10)$$

If the difference in Fermi potentials is ΔV_F for a material in which all of the nuclei are aligned, a neutron that interacts with N randomly oriented nuclei will experience an average potential difference of $\overline{\Delta V_F} = \Delta V_F / \sqrt{N}$. The number of interacting nuclei is $N \approx n(\lambda/2\pi)^3$, and, taking $\Delta V_F = V_F = 250 \text{ neV}$, $n = 10^{29} \text{ m}^{-3}$, $T_s = 130 \text{ s}$, $v = 6 \text{ m s}^{-1}$ and $l = 150 \text{ mm}$, a phase difference of

$$\Delta\phi \approx 0.02 \text{ rad} \quad (11)$$

is obtained. This implies that polarized neutrons can retain their polarization for times of the order of 10^5 s . In practice, the depolarization time in the storage trap used for this EDM experiment was of the order of 600 s.

It follows from the above that the ability to store polarized neutrons is exclusive to storage traps that are made of non-magnetic materials. If the walls of the trap contain magnetic domains of size comparable to or greater than the neutron wavelength, then the interaction of the magnetic moment of the neutrons with the magnetic field inside the domains dominates. Since the magnetic interaction can be a few hundred neV, the same size as V_F , one effectively suppresses the factor of $1/\sqrt{N}$ in the above calculation and the neutron polarization survival time drops to values of the order of 50 ms.

4. Ramsey’s method of separated oscillating fields

The precession frequency of the stored neutrons was determined by the method of separated oscillating fields. The method was devised for molecular beam experiments where an oscillating field is applied to the beam at the beginning and at the end of a flight path through an interaction region [59, 60]. In this EDM experiment, where the neutrons were stored in a trap, two short intervals of phase-coherent oscillating field were applied, one at the beginning and the other at the end of a period of free precession, so that they were separated in time but not in space. The phase coherence between the two pulses is achieved by gating off the output of a single oscillator during the intervening period. The sequence is shown schematically in Fig. 2.

At the start of each measurement cycle within a data-taking run, the neutrons passed through the magnetised polarizing foil and entered the storage volume with their spin polarization antiparallel to the uniform magnetic field \vec{B}_0 (a state referred to henceforth as “spin up”). A resonant oscillating field \mathbf{B}_1 , perpendicular to \mathbf{B}_0 and with a frequency close to resonance, was applied for 2 seconds with an amplitude such that the neutron polarization vector was rotated through an angle of $\pi/2$ and brought perpendicular to \mathbf{B}_0 . The polarization vector was then left to precess about \mathbf{B}_0 during a period T_{fp} (the subscript here indicating “free precession”), until the second phase-coherent oscillating field pulse was applied. If the oscillating field frequency had been

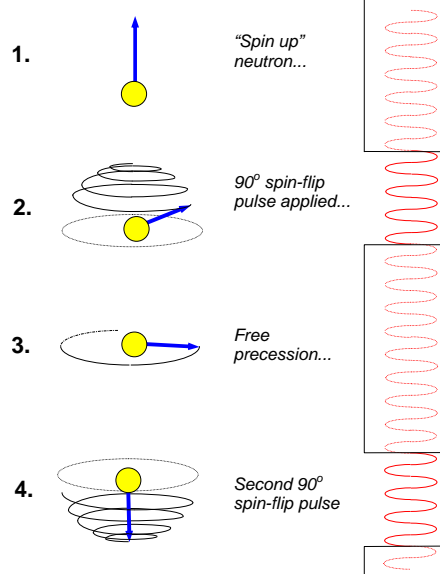


Figure 2: The Ramsey method of separated oscillatory fields. See text for description.

153 exactly on the center of the resonance, this second pulse would have rotated
 154 the polarization through a further $\pi/2$ such that it became parallel to \mathbf{B}_0 (the
 155 \hat{z} direction), as shown in Fig. 2. For frequencies a little off resonance, the final
 156 \hat{z} -component of the polarization depends strongly on the accumulated phase
 157 difference between the neutron polarization vector and the oscillator. When
 158 the neutrons were finally released from storage, the magnetised polarizing foil
 159 served as an analyzer, giving a neutron count that depended linearly upon this
 160 final \hat{z} component of the polarization. Thus, the neutron count was sensitive to
 161 the accumulated precession phase.

162 Emptying the trap and counting the stored neutrons took 40-50 s. For half of
 163 this time, a 20 kHz oscillating current was applied to a solenoid wrapped around
 164 the guide tube above the polarizer. This flipped the spins of the neutrons, and
 165 allowed the neutrons in the opposite spin state (“spin down”) to be counted.

Fig. 3 shows the Ramsey resonance pattern obtained experimentally as the
 frequency of the oscillating field \mathbf{B}_1 was varied. It is expected theoretically

[59, 60] that, across the central fringes, the number of neutrons counted as a function of the oscillating field frequency ν can be described by

$$N_{\uparrow\downarrow}(\nu) = \bar{N}_{\uparrow\downarrow} \mp \alpha_{\uparrow\downarrow} \bar{N}_{\uparrow\downarrow} \cos\left(\frac{\pi(\nu - \nu_0)}{\Delta\nu}\right), \quad (12)$$

where \bar{N} is the average number of neutrons counted for the spin state in question, up \uparrow or down \downarrow . The visibility α is the product of the neutron polarization and analyzing power, again for the spin state in question; ν_0 is the resonant frequency, and the linewidth $\Delta\nu$ is the width at half height of the central fringe. The two signs \mp also refer to the two spin states. \bar{N} and α (for either spin state) are related to the fringe maximum and minimum N_{\max} , N_{\min} as follows:

$$\begin{aligned} \bar{N} &= \frac{(N_{\max} + N_{\min})}{2}, \\ \alpha &= \frac{(N_{\max} - N_{\min})}{(N_{\max} + N_{\min})}. \end{aligned}$$

Given a time T_{fp} between the two oscillating field pulses, if the oscillating field is applied for a time t at both the beginning and the end of the storage time then the linewidth $\Delta\nu$ is given by [61]

$$\Delta\nu = \frac{1}{2(T_{fp} + 4t/\pi)} \quad (13)$$

$$\approx \frac{1}{2T_{fp}}, \text{ if } 4t/\pi \ll T_{fp}. \quad (14)$$

Eq. (12) may be differentiated to obtain

$$\frac{dN}{d\nu} = \frac{\pi}{\Delta\nu} \alpha \bar{N} \sin\left(\frac{\pi(\nu - \nu_0)}{\Delta\nu}\right). \quad (15)$$

The measurements were made at $\nu \approx \nu_0 \pm \Delta\nu/2$, where the number of neutrons counted was $N_{\uparrow\downarrow} \approx \bar{N}_{\uparrow\downarrow}$ for each spin state, giving a total of $N \approx \bar{N}_{\uparrow} + \bar{N}_{\downarrow}$ neutrons per measurement cycle. The fractional uncertainty in the number of neutrons counted is at best $1/\sqrt{N}$, so the uncertainty in the measurement of the frequency is no better than

$$\begin{aligned} \sigma_\nu &= \frac{\Delta\nu}{\pi\alpha\sqrt{N}} \\ &\approx \frac{1}{2\pi\alpha T_{fp}\sqrt{N}}. \end{aligned} \quad (16)$$

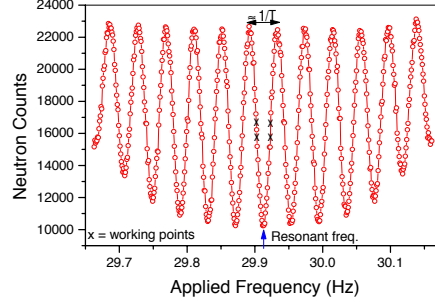


Figure 3: The Ramsey resonance pattern obtained by scanning the frequency of the oscillating field \mathbf{B}_1 through the resonance. The coherence time (between the Ramsey pulses) was 22 s in a $1 \mu\text{T}$ magnetic field. The ordinate is the number of neutrons in the original spin state counted at the end of each storage time. Error bars are omitted for clarity. During normal data taking measurements were taken sequentially at the four points shown.

In the case of a perfectly constant magnetic field, the EDM could be calculated from the difference in precession frequency between the two directions of the electric field. For a total (over a number of measurement cycles) of N_T neutrons, equally divided between the two directions of the electric field, the uncertainty in the EDM due to neutron counting statistics would be

$$\sigma_d \approx \frac{\hbar}{2\alpha E_0 T_{fp} \sqrt{N_T}}. \quad (17)$$

166 This result, which is applicable when the noise does not exceed that due to
 167 normal counting statistics, corresponds to the fundamental limit of sensitivity
 168 given by Heisenberg's uncertainty principle: the uncertainty in frequency is
 169 inversely proportional to the observation time T_{fp} .

170 It is desirable for the systematic error in absolute frequency to be as low as
 171 0.2 ppm. In the neutron case there is a significant upward shift created by the
 172 Ramsey-Bloch-Siegert (RBS) effect [62, 63]. In the EDM data taking cycle, this
 173 shift is calculated to be 0.15 ppm. Other systematic-error frequency shifts, such
 174 as that due to the rotation of the Earth, are discussed in [1] and [64].

175 One of the great virtues of the Ramsey method is the symmetry of the central
 176 fringe about the true Larmor frequency (plus RBS shift), even when the fringes

are smeared by field inhomogeneities. In this experiment the Ramsey pattern contained about 100 fringes, and the field was homogeneous to 0.1%.

Under normal running conditions, the magnetic field drifted slowly. However, the frequency measurements of the mercury magnetometer allowed us to set up a neutron resonance frequency on the synthesizer unfailingly extremely close to the desired part of the central fringe, and thereby to compensate for the magnetically induced frequency shifts within each measurement cycle. The precision of the Hg magnetometer was sufficient for the uncertainty on d_n to be dominated by neutron counting statistics, such that equation (17) still applies. Fig. 4 shows a typical set of data from a single run, fitted to the Ramsey curve. The spread of points along the curve arises from the shifts in the magnetic field from one batch cycle to another.

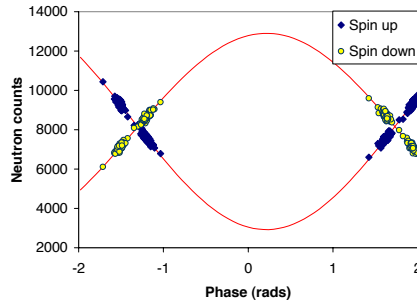


Figure 4: Spin-up and spin-down neutron counts for a single run fitted to the Ramsey curve (Eq. 12).

The data points of Fig. 5 show, on a log scale, the distribution (over the entire data set) of stretch values r_i of the fits to the Ramsey curve:

$$r_i = \frac{(\nu_i - \nu_{R_i})}{\sigma_i}, \quad (18)$$

where ν_i is the calculated frequency of the i th batch of neutrons, σ_i is its uncertainty and ν_{R_i} is the expected frequency for that batch as determined by the mercury magnetometer, the applied r.f. and the Ramsey curve function. Ideally, and in the absence of any EDM-like signals, this distribution would be expected

193 to be a Gaussian of unit width. The continuous line is a Gaussian of width
 194 1.06. The true distribution departs from this Gaussian at about 4σ . The few
 195 points lying outside this range tend to be associated with runs that have other
 196 known problems, for example with intermittent failure of the neutron delivery
 197 system. Because of the symmetric way in which the data were taken, rejecting
 198 batches that lie within the tails from this distribution cannot of itself induce a
 199 false EDM signal.

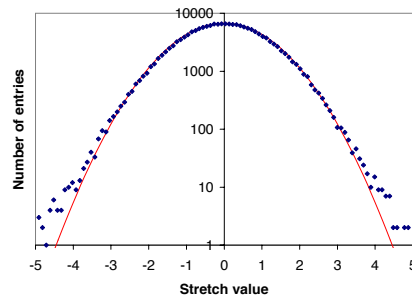


Figure 5: Distribution of stretch values from the fits to the Ramsey curve

200 5. Experimental apparatus

201 A schematic of the experimental apparatus is shown in Fig. 6.

202 5.1. The neutron subsystem

203 5.1.1. Neutron production and transport

204 Very cold neutrons with a speed of about 50 m/s are extracted from the
 205 liquid-deuterium cold source of the 58 MW high-flux ILL reactor, through a
 206 vertical guide known as the TGV (*tube guide verticale*). These neutrons are
 207 incident on the Steyerl turbine[65, 66] which converts them to UCN by reflection
 208 from the (receding) turbine blades. The UCN exiting from the turbine can be
 209 directed to several experimental positions by computer-controlled switching of
 210 horizontal UCN guides. At the entrance to the horizontal guide of the EDM
 211 position, the turbine blades produce a phase space density (PSD) of 0.084 UCN

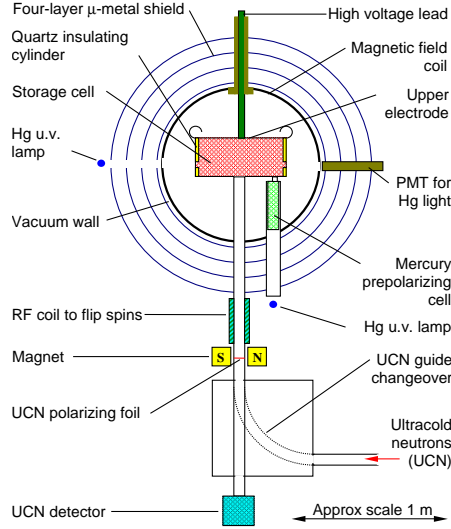


Figure 6: The neutron EDM experimental apparatus

212 $(\text{m/s})^{-3}\text{cm}^{-3}$, which remains constant up to a UCN velocity of 8 m/s, or an
 213 energy equivalent to 3.2 m fall in height. This PSD can provide 87 UCN/cm³ in a
 214 natural nickel bottle, 71 UCN/cm³ in a stainless steel bottle and 25 UCN/cm³ in
 215 a vitreous quartz bottle of height 0.12 m. The latter density is the most relevant
 216 since the sidewall of the EDM measurement bottle was made of vitreous quartz
 217 and was 0.12 m high. These numbers are ‘real UCN’[66] in that they do not allow
 218 for the reduction on conversion to counts caused by the efficiency 0.80 ± 0.05 of
 219 the UCN detector.

220 Following a lengthy shutdown for refurbishment, the ILL restarted in 1995.
 221 The flux from the neutron turbine was measured at that time and found to be
 222 reasonably consistent with the original measurements. Thereafter, our experi-
 223 mental data show it to have been in general reliable and consistent throughout
 224 the six-year data-taking period, with some long-term variation showing depar-
 225 tures in either direction of up to a factor of 1.5 from the average. This is reflected
 226 in Fig. 7, which shows the average number of neutrons per batch counted for
 227 each of our data-taking runs from 1998 to 2002. The general trend here was

228 also reflected in the count rate within a small detector monitoring the neutron
 229 density in the guide tube feeding the experiment; this latter is not shown here
 230 because of its far greater point-to-point scatter.

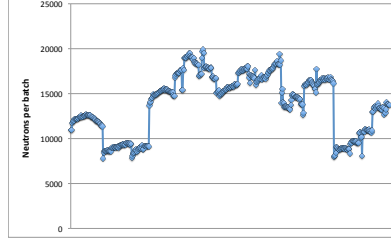


Figure 7: The average number of neutrons recorded per batch for each data-taking run.

231 The UCN guide from the turbine blades to the EDM bottle had a total
 232 length of 9.2 m divided into a horizontal length of 7.1 m followed by a vertical
 233 length to the upper surface of the lower electrode of 2.08 ± 0.05 m. This latter
 234 figure is the height above the UCN source of the DLC surface of the bottle lower
 235 electrode. Thus, UCN need to have an energy corresponding to 2.08 m of height
 236 at the source in order to only just reach the lower electrode surface, and to have
 237 an energy corresponding to 3.00 m of height at the source in order to enter the
 238 EDM bottle with the highest fully containable energy of 0.92 m at the lower
 239 electrode surface. This range of energies at the source is within the range of
 240 its uniform brightness. Thus a perfect 9.2 m of guide with no polarizer and no
 241 safety window in place, and no annihilation of UCN, would fill the EDM bottle
 242 to 25 UCN/cm³.

243 We have used diffusion theory[52] to model the filling of our bottle with the
 244 real guides and their losses. The guides had three types of surface: natural nickel
 245 evaporated onto thin glass for 1.8 m in the turbine house, with cross section 70
 246 mm x 70 mm; ⁵⁸NiMo sputtered onto electro-polished stainless steel surfaces for
 247 5.9 m from the turbine house to the position of the polarizer, with circular cross
 248 section of diameter 78 mm; and Be sputtered onto glass for the 1.5 m above the

249 polarizer to the EDM bottle, again circular in cross section, with a diameter
 250 of 65 mm. The theory indicates that at the completion of a long filling of the
 251 EDM bottle, the guide system, including the 0.1 mm thick aluminium safety
 252 window, is attenuating the PSD at the base of the bottle relative to that of the
 253 UCN source by a factor of 0.55 for the lowest energy UCN that can enter the
 254 bottle and by a factor of 0.22 for the highest energy UCN that can be contained
 255 in the bottle. This represents a considerable softening in the UCN spectrum
 256 in the bottle compared to a Maxwell spectrum with the quartz cut-off. There
 257 are three mechanisms involved in this softening. First, the UCN that can only
 258 just enter the bottle are on the point of marginally exceeding the lower (2.0 m)
 259 Fermi potential energy in the (ferro-magnetic) nickel surface of the guide in the
 260 turbine house. This energy excess increases to 1.0 m height equivalent at the
 261 top end of the bottle spectrum, and causes much leakage of these UCN through
 262 the nickel guide wall. The result is a 30% relative reduction in the UCN PSD
 263 at the top end relative to the bottom end of the bottle spectrum. Secondly,
 264 the performance of the entire guide system deteriorates with increasing UCN
 265 energy since both the UCN losses in guide wall reflections and their diffuse
 266 reflection probabilities increase with UCN energy. This results in a further 29%
 267 relative reduction in PSD at the top end. Lastly, the UCN current drawn from
 268 the guide by the UCN losses in the EDM bottle itself also increases with UCN
 269 energy, causing a relative reduction of 17.5%. When the polarizer is inserted,
 270 these last attenuations are slightly more than those just given.

271 The diffusion model just referred to has just one adjustable parameter, which
 272 represents the probability of diffuse reflection per collision for UCN with a total
 273 energy equal to the critical energy. All of the guide surfaces have thin sputtered
 274 or evaporated coatings on highly polished substrates. The parameter was ad-
 275 justed to give the observed number of UCN just after filling for our EDM bottle
 276 after five filling time constants. Agreement with experiment on UCN densities
 277 was therefore ensured. The probability of diffuse reflection per collision de-
 278 duced from the fit for UCN at the local critical energy was found to be 0.075.
 279 In independent experiments, we have found a corresponding value of 0.040 for

280 uncoated lightly electro-polished honed stainless steel surfaces. [67, 68] This
 281 suggests that coating processes increase the surface roughness for the surface
 282 wavelengths that are short enough to produce totally diffuse reflections. For
 283 UCN with an isotropic distribution of velocities and kinetic energy equal to half
 284 of the critical energy our probability of diffuse reflection per collision on the
 285 coated surfaces would be $0.075/2 = 0.038$. In the case of uncoated stainless
 286 steel this last figure would be 0.02.

287 The main value of the diffusion calculation has been the determination of
 288 the shape of the UCN energy spectrum used for the EDM measurement. The
 289 spectrum shape is important in understanding some of the later results. Al-
 290 though the softening of the spectrum reduces UCN numbers, it increases the
 291 average UCN storage time more than in proportion to the reduction of UCN
 292 energy. This largely cancels the reduction in sensitivity of the EDM measure-
 293 ment by allowing the use of a longer Ramsey resonance time. The softening
 294 also increases the average height difference due to gravity between the stored
 295 UCN and the stored Hg atoms. Knowledge of the UCN spectrum allows one to
 296 calculate this height difference, which is needed for a method of assessing the
 297 systematic errors caused by geometric phases.[51, 69] This height difference can
 298 also be determined using magnetic resonance, with a containment trap of vari-
 299 able height. This gives results in good agreement with that calculated from the
 300 UCN spectrum. This UCN spectrum is also successful in fitting the observed
 301 UCN counts versus storage interval for all intervals between 60 s and 600 s to
 302 within the RMS noise of about 2% arising from fluctuations in shutter timing.
 303 At zero containment time there appears to be a 25% UCN excess due to the
 304 presence of UCN that are not fully contained. At a containment time of 60 s
 305 these extra UCN appear to have fallen below the 2% noise level.

306 The spectrum-weighted average attenuation of the PSD in the EDM bottle
 307 filling process was a factor of 0.295 relative to the UCN source. This led to
 308 an initial density of fully contained UCN in the bottle, after a long filling time
 309 with no polarizer and on just closing the door, of 7.5 fully contained UCN/cm³
 310 and a total number of 160,000 UCN. The latter number falls to 69,400 after

311 the containment interval of 140 s used when taking EDM data. To find the
 312 final UCN counts from an EDM data-taking cycle we must take account of
 313 further attenuations to the figure of 69,400 per batch. These are (i) 0.727 for
 314 curtailment of the filling and emptying intervals to conserve polarisation and
 315 batch cycle duration (ii) 0.525 for spin selection, which includes a small increase
 316 due to production of wrong spins (iii) 0.80 for the combined loss in two transits
 317 of the polarizer foil (iv) 0.875 for losses when waiting for the spin flipper while
 318 the other spin state is counted (v) 0.915 for guide losses in transit from the
 319 bottle to the detector (vi) 0.80 for detector efficiency. These figures indicate a
 320 final count of 13,600 per batch - close to the 14,300 observed average count from
 321 all runs.

322 We believe that the spectrum changes derived from these last attenuations
 323 are small and partly cancelling - process (i) gives a slight hardening (ii) and (iii)
 324 and (vi) are neutral while (iv) and (v) induce a slight softening.

325 In order to deal with the variety of surfaces involved, a simple model has
 326 been adopted for estimating the parameter η to be used with the theoretical
 327 energy dependence in calculating the UCN loss probability per collision. Our
 328 model takes $\eta = (\eta_A + \eta_H)$, where η_A is the contribution for the atomic com-
 329 position of the material excluding hydrogen and η_H is the contribution from
 330 interstitial hydrogen. We are concerned with the situation where none of the
 331 materials has been baked in vacuum. From measurements on 316-type stain-
 332 less steel[70] we take $\eta_H(\text{SS})$ to be 3.9×10^{-4} and for other materials X we take
 333 $\eta_H(X) = \eta_H(\text{SS}) \times (V_{\text{SS}}/V_X)$, where the V s are the mean Fermi potentials. This
 334 amounts to assuming that, at room temperature, the atomic fraction of hydro-
 335 gen and the UCN loss cross-section for hydrogen are the same in the surface
 336 layers of all the materials concerned. In our experience this model works well
 337 in predicting lifetimes to about 20% in wide variety of bottles and guide tubes
 338 made of unbaked materials at room temperature.

339 The key data used in this assessment arose from a data-taking run labelled
 340 ALP1120.dat, which produced data for UCN counts versus containment time
 341 in steps of 5 s up to 660 s. It used a large smooth-sided bottle with a period of

342 60 s used for filling and 70 s for emptying, with no polarizer present. Only the
 343 emptying process enters to cause the data count totals to differ from the actual
 344 number of real UCN in the bottle when the shutter is opened for emptying. This
 345 difference involves just two factors: (i) the detector efficiency, and (ii) UCN lost
 346 in the emptying guide and in the bottle after the shutter is opened. The detector
 347 efficiency is generally assessed as 0.80 ± 0.05 , with losses in the window and loss
 348 of counts below the discrimination level each being about 0.10. The overall
 349 emptying time constant after 140 s of containment was measured in a separate
 350 run, labelled ALP1115.dat, to be 9.35 ± 0.30 s. After this containment, the bottle
 351 UCN lifetime is about 210 s, so the fractional bottle loss during emptying is to
 352 first order $9.4/210 = 0.045$. To calculate losses in the guide we need the average
 353 time spent in the guide by each UCN before it is detected, and the storage time
 354 of the guide. The latter is typically 20 s. If the guide were to be perfectly
 355 smooth the time to the detector would be the free-fall time, which is 0.4 s;
 356 however, the guide has some roughness, and we can estimate from the emptying
 357 time constant that about 40 % of the UCN that leave actually return to the
 358 bottle. Assuming that the roughness approximately doubles the time taken,
 359 making 0.8 secs, the fractional loss would be $0.8/20 = 0.04$, making a total
 360 emptying loss of $0.045 + 0.04 = 0.085$. We are now in a position to calculate the
 361 real number of stored UCN. Then, knowing the turbine performance[65, 66],
 362 we have the overall loss in the entry guide system, which allows us to fix the
 363 roughness parameter.

364 5.1.2. *The neutron polarizer*

365 The neutrons were polarized by transmission through a silicon foil upon
 366 which was deposited a $1 \mu\text{m}$ layer of iron that was magnetised close to saturation
 367 by a field of about 0.1 T from a permanent magnet. This had Fermi potentials
 368 of approximately 90 and 300 neV for the two spin states of the neutron. The foil
 369 was mounted 1.5 m below the trap, so that neutrons that had sufficient energy
 370 to penetrate the foil could slow down before reaching the trap.

371 The polarizer was mounted with the magnetized layer towards the trap,

372 since experience in the past showed that this orientation gave the better neutron
 373 polarization. With neutrons that made a single passage through the foil, such
 374 polarizers can produce a transmitted neutron polarization in excess of 90% [71].
 375 However, they do have a finite probability, of a few percent, of flipping the
 376 spin of both transmitted and reflected neutrons. In this case it led to a build-
 377 up of neutrons in the unwanted spin state as the trap filled, thus reducing the
 378 polarization that was finally achieved. The maximum polarization was obtained
 379 for very short filling times [72]. The filling time was therefore adjusted so as to
 380 maximize $\alpha\sqrt{N}$.

381 As mentioned above, the 1.5 m of neutron guide between the polarizer and
 382 the neutron trap was made of glass, with the inner surface coated with BeO,
 383 which is non-magnetic. This guide was used instead of a stainless steel guide
 384 because remnant magnetization and magnetic domain structure in a stainless
 385 steel guide would have caused severe inhomogeneity in the B_0 field as well as
 386 causing depolarization of the neutrons in wall collisions. The use of glass also
 387 allowed the penetration of the oscillating magnetic field of the spin flip coil, at
 388 20 kHz. This coil was used towards the end of the measurement cycle, when
 389 the spin-down neutrons were emptied from the trap and counted.

390 To prevent depolarization as the neutrons passed from the magnetic field
 391 of the polarizer, through the Earth's 60 μ T magnetic field, and into the 1 μ T
 392 magnetic field of the trap, a variable-pitch solenoid was wound around an 18-cm-
 393 diameter former concentric with the guide tube. This ensured that the magnetic
 394 field changed smoothly and monotonically, and that there is no zero-field region
 395 along the guide.

396 *5.1.3. The neutron storage trap*

397 The neutron storage trap was made of two flat, 30 mm thick, circular alu-
 398 minum electrodes, separated by a hollow right circular cylinder of quartz that
 399 also acted as a high-voltage insulator. The electrodes had aluminum corona
 400 domes attached, and the insulator was recessed 15 mm into the electrodes to re-
 401 duce high-voltage breakdown [73]. At the bottom of the recess in each electrode,

402 a Teflon O-ring was housed to provide a gas-tight seal between the electrode
403 itself and the inner surface of the quartz ring, so as to contain the polarized
404 atomic mercury used for the magnetometry, as described in Section 5.2.

405 About halfway through the data-taking period, the existing smooth-walled
406 quartz cylinder was replaced by another quartz cylinder of the same inner di-
407 mensions but with a matt surface finish. These are referred to as the smooth
408 and rough traps respectively.

409 Bare aluminum has a Fermi potential of 55 neV (corresponding to a critical
410 velocity of 3.3 m/s). Aluminum oxide surfaces quickly depolarize any mercury
411 that comes into contact with them. The electrodes are therefore coated with
412 a thin insulating layer of a relatively high Fermi potential material. Initially,
413 Teflon was used for this purpose; it was sprayed on, and baked in an oven.
414 However, it did not adhere well enough to the surface, and it eventually peeled
415 away, causing high-voltage sparks to the resulting loose Teflon flaps. The Teflon
416 was then replaced by a 1 μm thick coating of diamond-like carbon (DLC),
417 produced by chemical vapor deposition from a plasma discharge in deuterated
418 methane [74], which proved to be far more durable. The Fermi potential of this
419 layer is 220 neV. The quartz insulator has a Fermi potential of 91 neV. All of
420 the data analysed in this paper were taken with the DLC-coated electrodes.

421 The trap had an interior diameter of 470 mm and a height of 150 mm. The
422 15 mm recess in each electrode yielded a distance between the electrodes, for the
423 majority of the surface, of 120 mm. The overall volume was therefore 21 liters.

424 The annular quartz insulators forming the sidewalls, which were machined
425 from single pieces of fused silica, had a 15 mm wall thickness. A Suprasil window
426 in either side allowed the passage of a beam of polarized 2537 Å light, which was
427 used to probe the state of polarization of the mercury atoms as they precessed
428 in the \mathbf{B}_0 field.

429 The lower electrode was electrically grounded, and had a 67 mm diameter,
430 4 cm deep hole in the center, through which the neutrons enter the trap. The
431 hole could be closed by a sliding DLC-coated beryllium-copper door that had
432 been adjusted to have gaps of less than 100 μm . This non-magnetic door slid

on nylon bearings and it was operated by a mechanical coupling from a remote piston driven by compressed air. A second hole in the electrode, of diameter 10 mm, gave access to a door that opened for 1 s during the measurement cycle to allow the polarized mercury to enter the trap.

The neutron-trap support system, door mechanism, mercury polarizer and all other items inside the vacuum vessel were made from non-ferromagnetic materials. Materials such as brass were avoided because they often contain ferromagnetic impurities. Scans with a fluxgate magnetometer of sensitivity 1 nT approaching to within 2 cm of the inner surface of the storage volume revealed no magnetic anomalies.

5.1.4. *The neutron detector*

The neutron detector was a proportional counter containing 1200 mbar of argon, 50 mbar of ^3He and 100 mbar of methane, in which the neutrons were detected via the reaction



which releases 764 keV of energy. The central electrode was a loop of tungsten wire of diameter 200 μm and was maintained at 2.5 kV [67].

The window of the detector was a 100 μm aluminum foil, with a mean Fermi potential of 55 neV. The detector was placed 2 m below the neutron trap to ensure that nearly all the neutrons reaching it, after falling freely through the Earth's gravitational field, have a sufficiently large velocity component perpendicular to the window to penetrate it. The efficiency of the detector was about 80% for UCN. The detector was shielded by 150 mm of polyethylene and 5 mm of boron-loaded plastic resulting in a background *in situ* of less than one count in 10 s, whereas the average UCN count after a single four-minute measurement cycle was about 14,000 in 40 s for this data set.

5.2. *The mercury magnetometer*

The construction and performance [75] of the atomic mercury magnetometer (Fig. 8) have been discussed elsewhere. Here a brief account is given of its use

458 in the EDM experiment.

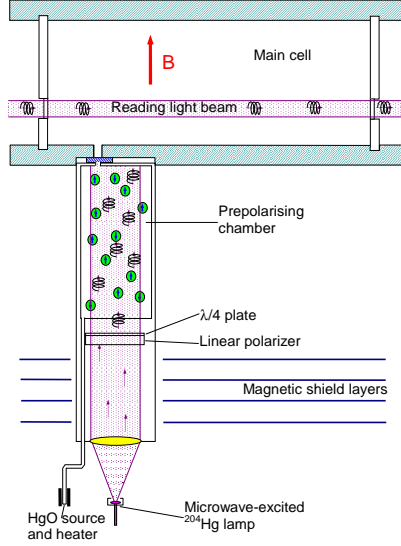


Figure 8: Diagram of the mercury magnetometer

459 5.2.1. Principle of operation

460 Spin-polarized ^{199}Hg atoms were made to enter the storage volume once it
 461 had been filled with neutrons and the neutron entrance door had been closed.
 462 A rotating magnetic field \mathbf{B}'_1 , perpendicular to the main \mathbf{B}_0 field, was applied
 463 for a period of 2 s. The \mathbf{B}'_1 field had a frequency equal to the spin preces-
 464 sion frequency of the mercury atoms – 7.79 Hz – and was of the appropriate
 465 strength to turn the spin polarization vector by $\pi/2$ radians into the xy plane
 466 perpendicular to \mathbf{B}_0 . Meanwhile, a beam of 2537 Å polarized light from an
 467 isotopically-pure ^{204}Hg discharge tube (which has good spectral overlap with
 468 the ^{199}Hg) traversed the chamber. The absorption of this light depended upon
 469 the x component of polarization of the mercury atoms, and thus varied with time
 470 as an exponentially-decaying sinusoid. The intensity of the light was monitored

471 by a solar-blind Hamamatsu R431S photomultiplier tube, the output current of
 472 which was converted into a voltage, passed through a bandpass filter, and digi-
 473 tised with a 16-bit ADC at a rate of 100 Hz. The absolute value of the photon
 474 flux was not measured, but was probably of the order of 10^{12} to 10^{13} per second
 475 – the intensity was low enough that its contribution to the relaxation in the
 476 measurement cell was not significant. The noise on the signal was determined
 477 by shot noise on the photon flux. The voltage applied to the PMT, and thus its
 478 gain, was left unchanged throughout the six years of data taking.

479 The resulting data from each batch of mercury (Fig. 9) were fitted to obtain
 480 the average frequency, as described in Section 5.2.4; and hence the volume-
 481 and time-averaged magnetic field during the Ramsey measurement interval was
 482 calculated. At the end of the storage period the mercury atoms were pumped
 483 out of the cell via the neutron entrance door.

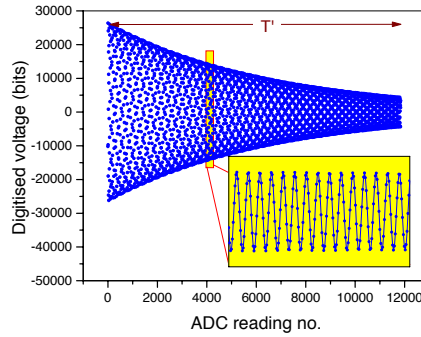


Figure 9: A set of mercury ADC readings from one measurement cycle. The gradual depolarization is clearly visible, and the expanded region shows the underlying 8 Hz precession frequency. The frequency measurement period T' excludes a two-second settling period at the start.

484 5.2.2. Mercury source, polarizer and analyzer

485 The mercury source was a powder of ^{199}HgO , which was dissociated by
 486 continuous heating to approximately 200 °C. After passing through a narrow
 487 Fomblin-grease coated pipe, the mercury atoms reached a 1.2 liter chamber sit-

uated adjacent to the main neutron storage volume, within the $1\ \mu\text{T}$ \mathbf{B}_0 field. There they were optically pumped by light from a ^{204}Hg discharge lamp, identical to that used for monitoring the polarization within the neutron storage volume. The pumping process was continuous, so that as each charge of polarized atoms entered the storage volume for the frequency measurement the next charge began to build up and polarize. Typically the mercury density within the pumping cell was such that there were about two absorption lengths for the 254 nm line from the ^{204}Hg discharge lamp. The relaxation time of the pumping cell in darkness was about 70-90 s.

The discharge lamp lay one focal length below an 80 mm diameter f2 lens (which also served as a vacuum window). The photon flux after this lens was estimated to be typically about 7×10^{13} per second: somewhat higher, for geometrical reasons, than that of the light used to monitor the precession. The parallel beam of light emerging from the lens passed through a linear polarizer followed by a quarter-wave plate to produce the necessary circular polarization. The analyzing, or reading, light followed a similar arrangement.

5.2.3. Absorption and polarization characteristics

The absorption A of the reading light, which was proportional to the number of mercury atoms within the chamber, is defined as

$$A = \frac{I_0 - I_1}{I_0}, \quad (20)$$

where I_0 and I_1 are the DC levels of the reading light measured just before and just after, respectively, the injection of polarized mercury into the main storage volume. The initial amplitude a of the oscillating signal is related to the polarization P as [75–77]

$$a = I_1 \left\{ (1 - A)^{-P} - 1 \right\}, \quad (21)$$

so the level of polarization may be extracted simply from the absorption and the fitted signal amplitude.

The polarization is found to depend strongly upon A because, in the polarizing chamber, the probability of absorbing a reemitted photon increases

quadratically with the density of mercury. Secondary, and higher order, reabsorptions increase even more quickly. A large charge of mercury therefore yields a relatively small polarization. One finds empirically that

$$P \approx p_1 \exp(-A\alpha), \quad (22)$$

where p_1 and α might typically have values of around 0.5 and 6 respectively. The function (21) is maximized at an absorption of approximately 16%, and this therefore provides the optimum signal-to-noise ratio. The temperature of the mercury source was adjusted periodically in order to try to keep the absorption fairly near this value.

5.2.4. Calculation of precession frequency

As with other aspects of the magnetometer, the frequency fitting procedure has been discussed in some detail in [75], and it is therefore only briefly described here.

The AC component of the mercury signal was amplified so as to match the input voltage range of the ADC used for its digitisation. The clock pulses that trigger the ADC readings were gated off while the mercury entered the chamber and while the $\pi/2$ pulse was applied, and readings for an additional 2 s after that time were ignored in case they were influenced by transient effects. The readings were, however, recorded throughout the 20 s neutron filling period, during which time there was no mercury in the storage cell. This allowed the evaluation of the rms noise on the signal, from which an estimator of the uncertainty of each reading in the fit could be deduced.

Because the magnetic field drifted with time, the frequency changed slightly during the measurement. Therefore, instead of fitting the entire array of ADC readings to a decaying sinusoid, a pair of shorter ($t = 15$ s) intervals at either end of the Ramsey measurement period were fitted in order to find the phases at points close to the beginning and the end [78]. The total phase difference (including $2n\pi$ for the complete cycles) divided by the time gives the average frequency, and hence the time- and volume-averaged magnetic field for the interval

532 of free precession.

533 The fitted function generally appeared to describe the data well, with the
 534 χ^2/ν distribution peaking close to 1.0, as shown by the data points in Fig. 10.

535 The distribution shown in Fig. 10 is truncated at $\chi^2/\nu = 4.5$. If χ^2/ν
 536 > 4 , however, the online fitting procedure attempts to correct for potential
 537 hardware errors such as missed clock cycles, sticking bits, saturation, too-short
 538 depolarisation time, and/or occasional sparks. The discontinuity at 4.0 reflects
 539 the fact that the majority of the fits with originally larger χ^2/ν were incorrect,
 540 and they have successfully been re-fitted with an appropriate correction for one
 541 or more of these problems.

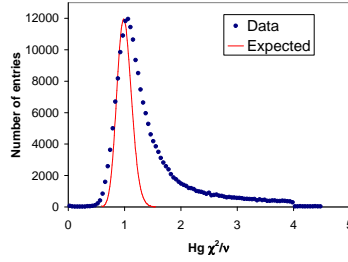


Figure 10: Distribution of χ^2/ν for approximately 205,000 fits of the mercury precession frequency, together with the expected distribution for the ideal case of no magnetic field drift.

542 5.2.5. *Effects of the bandpass amplifier*

543 The mercury frequency fitting routine assumed no correlations between the
 544 individual ADC readings. The measured rms noise was used as an estimate of
 545 the uncertainty of each point. Prior to digitization, however, the mercury signal
 546 was filtered by a bandpass amplifier with a Q of approximately 5.9 in order to
 547 reduce the noise; consequently, neighbouring ADC measurements are actually
 548 rather strongly correlated with one another, and the calculated variance must
 549 be modified to allow for this.

550 If the points were independent, the variance σ^2 of the fitted frequency would
 551 be expected to be inversely proportional to the number of readings $n = 3000$

552 obtained in the short intervals at either end of the signal train, as shown in
 553 ref. [75]. When the data are correlated, this is no longer true; for a given
 554 bandwidth, increasing the sampling frequency beyond a certain point does not
 555 reduce the variance. The calculations in [78] suggest that that point is reached
 556 when $n_s Q = 3$, where n_s is the number of readings taken per period. In the
 557 case of this experiment, $n_s = 12.5$ and $Q \approx 5.9$, giving an overall factor of
 558 74, i.e. approximately 25 times above this limit; thus the true variance on the
 559 frequency determination is expected to be higher than the naïve estimate by
 560 the same factor of 25.

561 This hypothesis was tested by adding white noise to a precise 8 Hz synthe-
 562 sized signal from a frequency generator, and performing a series of fits of the
 563 frequency of the resulting signal, firstly with and then without the bandpass
 564 filter in place. With a flat response, the spread in the measured frequencies
 565 was consistent with a Gaussian random distribution about the mean, having
 566 $\chi^2/\nu = 1.0$. With the bandpass filter, the noise was reduced by a factor of five,
 567 as was the estimated uncertainty of each fitted frequency; but the scatter in the
 568 results increased, with χ^2/ν rising to 25, suggesting that the error bars were
 569 indeed a factor of five too small. Furthermore, this same factor is consistent
 570 with the scatter observed in the experimental data during periods when the
 571 magnetic field is stable, and it also agrees with estimates based upon numerical
 572 simulations using a digital Butterworth filter.

573 In the discussions that follow, all calculated uncertainties in the mercury pre-
 574 cession frequency incorporate a factor of 5.0 (i.e., a factor of 25 in the variance)
 575 to allow for this narrow-banding effect.

576 This same effect also broadens the χ^2/ν distribution. The expected distri-
 577 bution, shown as a smooth curve in Fig. 10, is therefore that appropriate to
 578 $3000/25 = 120$ degrees of freedom. As the magnetic field during each measure-
 579 ment period drifts slightly, the frequency is not perfectly constant. The true
 580 distribution is therefore expected to broaden further, particularly on the high
 581 side. There is a reasonable match on the low side, and the position of the peak

582 is close to unity.

583 5.2.6. Performance of the magnetometer

584 As with the neutrons, it is desirable that the absolute precision of the mer-
 585 cury frequency measurements should be better than 0.2 ppm. In Section 5.2.11
 586 we discuss possible mechanisms that could affect the accuracy of this system.

587 Fig. 11 shows a typical example of the evolution of the magnetic field, as
 588 measured by the mercury precession frequency, throughout a typical run. Error
 589 bars, which are of the order of a microhertz, are smaller than the points them-
 590 selves on this plot. The drift in magnetic field during this time is approximately
 591 5×10^{-11} T. For this run an electric field of magnitude 4 kV/cm was applied to
 592 the storage volume, with its polarity reversing approximately every 70 minutes.

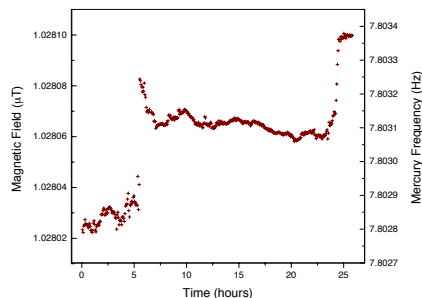


Figure 11: Magnetic field strength, as determined by the mercury resonant frequency, measured repeatedly over a 26-hour period.

593 Fig. 12 shows the corresponding series of measurements of the neutron res-
 594 onant frequency throughout the same 26-hour period. As expected, the same
 595 drift in magnetic field is reflected in this set of data. Error bars are again omit-
 596 ted for clarity, but are of order 29 μ Hz for this particular data set. The ratio of
 597 neutron to mercury frequencies, normalised to the mean neutron frequency —
 598 i.e., the measured neutron frequency corrected for the magnetic field drift — is
 599 shown on the same plot, where it appears as a flat line. The uncertainty on each
 600 point is approximately one part per million, giving a χ^2/ν of 0.89; this is con-
 601 sistent with the width of the line being entirely dominated by neutron counting

602 statistics. Any change in the neutron resonant frequency due to the interaction
 603 of the electric field with the neutron EDM would appear as a change in this
 604 ratio of frequencies. A straight-line fit to the ratio as a function of the applied
 605 electric field therefore yields a slope that is directly proportional to the EDM
 606 signal. It is evident that the use of this magnetometer compensates extremely
 607 efficiently for the large-scale effects of magnetic-field drift.

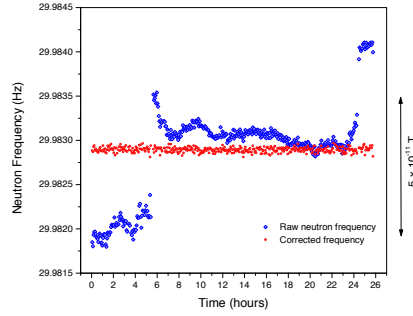


Figure 12: Neutron resonant frequency, measured over the same 26-hour period, before and after correction of the effect of the drifting magnetic field by normalisation to the measurements of the mercury magnetometer.

608 5.2.7. *Mercury frequency uncertainty*

609 The fitted Hg frequency sometimes has a relatively large uncertainty, partic-
 610 ularly if the depolarization time is short. The distribution of these uncertainties
 611 is shown in Fig. 13; a typical value is 1-2 μHz . For comparison, the typical
 612 inherent neutron frequency uncertainty from counting statistics was about 20
 613 μHz , corresponding to about 5 μHz in the mercury system.

614 5.2.8. *Magnetic field jumps*

615 The distribution of Hg frequency jumps, i.e. the difference in Hg frequency
 616 between a given batch and the previous batch, is shown in Fig. 14. There are
 617 broad tails due to occasional sudden changes in field, for example due to the
 618 movement of an overhead crane or to a mechanical disturbance to the μ -metal
 619 shields.

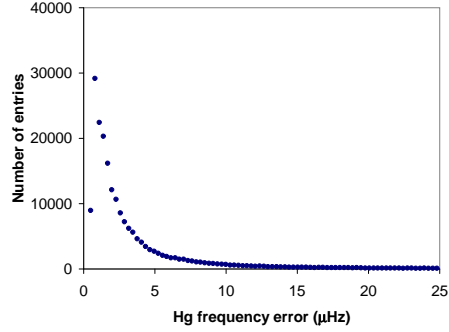


Figure 13: Distribution of uncertainties of the fitted Hg precession frequency

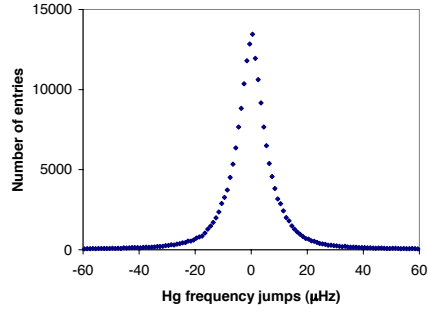


Figure 14: Distribution of changes in the Hg frequency from one batch cycle to the next

620 The mercury and the neutron frequency measurements do not have perfect
 621 temporal overlap. One can consider the start and end of the Hg measurements to
 622 be centred on the 15-second averaging period at the start and end of the Ramsey
 623 measurement time, whereas the neutrons average over all but 2 seconds at either
 624 end. If the field is changing, there is therefore a roughly 7-second period - i.e.
 625 about 1/30 of the total batch period - for which the change is not properly
 626 accounted. For comparison, a frequency jump of $60 \mu \text{ Hz}$ - which would be
 627 regarded as extreme - corresponds to a field jump of about 7.5 ppm, or just over
 628 1/20 of the Ramsey linewidth. With the aforementioned protection factor of
 629 1/30, this corresponds to a potential error in the frequency ratio R of 0.25 ppm,
 630 to be compared with a typical statistical uncertainty on the neutron frequency

631 of about 0.7 ppm.

632 5.2.9. Depolarization in strong electric fields

633 The depolarization time of the mercury depended strongly upon the high
634 voltage behavior of the storage cell. As the upper electrode was charged up,
635 the mercury depolarization time dropped precipitously, after which it slowly
636 recovered over a timescale of about an hour. Discharging and recharging at the
637 same polarity had little effect, but charging at the opposite polarity once again
638 shortened the depolarization time. During a normal EDM run, the polarity
639 was reversed about once per hour. The depolarization times therefore followed
640 a characteristic pattern of a series of rapid falls followed by slow recoveries,
641 upon which was superimposed a gradual overall reduction, as shown in Fig. 15.
642 Sparks also caused a rapid depolarization, from which there was only partial
643 recovery.

644 This effect of a temporary increase in relaxation each time the HV polarity
645 is reversed may be due to protons (H^+ ions) appearing on the newly positive
646 electrode. Electron migration in the dielectric surface layer soon takes over, and
647 the protons diffuse back into the surface layers again with a characteristic \sqrt{t}
648 dependence as the HT dwell progresses. Protons are believed to catalyse the
649 mercury depolarisation by forming the paramagnetic short-lived (10^{-6} s) HgH
650 molecules in surface encounters.

651 The depolarization time could be restored to a large extent by a high-voltage
652 discharge in 1 torr of oxygen; it was normally necessary to carry out this pro-
653 cedure every 1-3 days. Prior to this cleaning, the system was usually “trained”
654 by increasing the voltage to a fairly high value (between 120 and 170 kV) and
655 allowing it to settle until it could stay for several minutes without discharging,
656 as discussed in Section 5.4 below. Cleaning the quartz ring and then heating
657 it in 10^{-2} torr of He at 60 °C for about two days was also beneficial to the
658 depolarization time; this procedure was carried out between reactor cycles.

659 This detrimental effect of the high voltage upon the mercury depolarization
660 time could result in a false EDM signal if (a) the average depolarization time

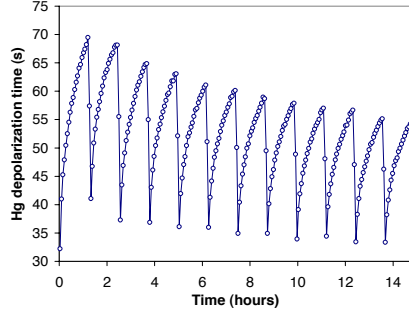


Figure 15: Behavior of the mercury depolarisation time during repeated reversal of the applied electric field.

were different for the two HV polarities, and (b) the mercury frequency had some small dependence upon the depolarization time. The cycle-by-cycle dependence of the neutron-to-mercury frequency ratio R upon the mercury depolarization time τ was found to be $\partial R / \partial \tau = (-0.5 \pm 3.2) \times 10^{-4}$ ppm per second for negative HV and $(+2.2 \pm 3.3) \times 10^{-4}$ ppm per second for positive HV, with an overall average of $(+0.9 \pm 2.3) \times 10^{-4}$ ppm per second. Coupled with a difference in average depolarization times (where the average has been calculated by weighting with the EDM measurement uncertainties) of $\tau_- - \tau_+ = 2.0 \pm 0.2$ s, an average effective neutron frequency shift above 12 nHz may be excluded at 90% CL. Such a frequency shift might conceivably contribute a false EDM signal of up to 1.2×10^{-27} e cm. However, this effect will cancel upon reversal of the magnetic field. As the quantities of data (as measured by the statistical uncertainty) for the two field directions were identical to within 1%, an error from this source is excluded at the level of 1.2×10^{-29} e cm.

This behavior of the mercury strongly constrained the sensitivity of the experiment, as it limited the magnitude of the electric field to a value substantially below the limit that could be set by leakage currents alone.

678 5.2.10. Mercury light shift

679 The presence of the Hg reading light, via the Ramsey-Bloch-Siegert mech-
 680 anism [62, 63], shifts the resonant frequency of the Hg atoms. These so-called
 681 light shifts are produced [79, 80] by any small component, parallel to \mathbf{B}_0 , of
 682 the ^{204}Hg probe light beam passing through the precessing ^{199}Hg atoms. This
 683 component (and the consequent shift in the neutron-to-mercury frequency ratio
 684 R) reverses sign on reversal of \mathbf{B}_0 . An effect of this kind, if present, is expected
 685 to be of the order of a fraction of a part per million. A slight dependence of
 686 R on the incident light intensity was indeed observed in this apparatus, the
 687 magnitude ~ 0.2 ppm being in agreement with theory. Any changes in intensity
 688 correlated with the electric field direction would then result in a frequency shift
 689 that would mimic an EDM. This is the direct light shift discussed in [1]. It
 690 is possible to modify the optics to reduce the amount of light travelling in the
 691 direction parallel to B_0 , and in fact this has recently been carried out by the
 692 current users of this apparatus. Here we describe the analysis carried out in
 693 order to evaluate the light-shift effect within our data.

694 Although we do not have precise spectral information about the reading-
 695 light beam, it can contain several different wavelength components, only one of
 696 which serves to measure the ^{199}Hg precession. The raw intensity I_0 of the light,
 697 as measured by the PMT, cannot therefore be used to measure any effect of
 698 intensity upon R . Instead, the amplitude a of the AC component of the light
 699 was used; but it was necessary first to correct it for the absorption that it has
 700 undergone en route to the PMT.

The signal amplitude as a function of the absorption A and polarization P
 is approximately [75] (c.f. Eq. 20)

$$a = I_0 (1 - A) \left[(1 - A)^{-P} - 1 \right]. \quad (23)$$

701 As discussed above in Section 5.2.3 the polarization achieved depends in
 702 turn upon the quantity of ^{199}Hg within the trap, due to the relaxing effect of
 703 reemitted photons: the probability of absorbing a reemitted photon increases
 704 linearly with the Hg density. Secondary (and higher) reabsorptions increase

705 even more quickly. In consequence, P has an exponential dependence upon A
706 as given in Eq. 22.

707 This analysis was restricted to polarizations between 5% and 40%, and to
708 absorptions greater than 5%, for which this parameterization is appropriate.

709 Combining equations 23 and 22 yields an approximate analytic form for the
710 characteristic shape of the amplitude as a function of absorption, as shown in
711 Fig. 16. (This is a copy of Fig. 4 of [75], except that in the latter the y axis
712 is mislabelled “Polarisation” instead of “Amplitude”.) The function peaks at
713 approximately 16% absorption over a wide range of light intensities. Therefore,
714 although the *measured* amplitude of the signal may lie anywhere along this curve
715 depending upon the fraction of light absorbed, the peak value of this function,
716 which we denote a_{16} , should be a reasonably reliable measure of the *actual*
717 amplitude of the light incident upon the cell.

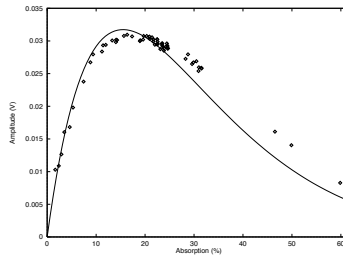


Figure 16: Amplitude of the AC component of the mercury light signal, as a function of the absorption.

Within any given data-taking run, the magnetic field configuration was never changed. Inevitably, though, the light intensity, the polarisation and the absorption would vary over time, and there was thus the potential for a change in R arising from the light shift. Our procedure therefore began by fitting the data within each run to Eq. 22, and thus determining the characteristic value P_{16} of the polarisation that corresponded to 16% absorption. The absorption-corrected

amplitude a_{16} for any A and P within that run is then (Eq. 23) given by

$$a_{16} = a \frac{0.84 (0.84^{-P_{16}} - 1)}{(1 - A) \{(1 - A)^{-P} - 1\}}. \quad (24)$$

For each batch cycle within a run, a measure could thus be obtained of the parameter a_{16} that corresponds to the amplitude of incident (resonant) light for that batch. A linear fit was then made for each run to establish whether there was a dependence of R upon a_{16} , which would be characteristic of the light shift. Over the six-year period of data taking for which this apparatus was used, two separate neutron traps were used: one had a rough wall, the other smooth. A weighted average of the resulting slopes was calculated for each of these two traps and for each direction of \mathbf{B}_0 .

The consistency of observed results suggested that it was appropriate to average the results from the two field directions, to obtain a magnitude of 0.21 ± 0.08 ppm/V for the rough trap. The results for the smooth trap, 0.01 ± 0.03 ppm/V, were consistent with zero. It was then possible to correct the rough-trap data for this effect on a run-by-run basis, using the average a_{16} for the run in question. We hypothesize that specular reflection within the smooth trap resulted in some cancellation of the effect, but we cannot know for certain; we rely upon our data-driven approach.

The amplitude a_{16} was also observed to have a slight dependence upon the applied HV, as follows:

- For \mathbf{B}_0 up: $\partial a_{16}/\partial V = 4.7 \pm 1.2 \times 10^{-6}$ volts per kV of applied HV
- For \mathbf{B}_0 down: $\partial a_{16}/\partial V = 11.0 \pm 1.6 \times 10^{-6}$ volts per kV of applied HV
- Average: $\partial a_{16}/\partial V = 8 \pm 1 \times 10^{-6}$ volts per kV.

However, since this dependence was corrected to within its uncertainty, no net bias should arise from this source. There remains an uncertainty on the dependence of R on the HV of $(\partial a_{16}/\partial V) \times (\partial R/\partial a_{16}) = 3 \times 10^{-7}$ ppm per applied kV when averaged over both data-taking traps. Since the light-induced frequency shift changes sign with B , this effect will not cancel upon reversal

of \mathbf{B}_0 . For a trap of height $H = 12$ cm this effect therefore contributes an uncertainty of

$$\frac{h}{2} \frac{\partial \nu}{\partial E} = \frac{h\nu}{2} \frac{\partial R}{\partial V} H = 2 \times 10^{-28} \text{ e cm.} \quad (25)$$

739 5.2.11. Accuracy of Hg frequency measurements

740 A number of mechanisms can affect the frequency measurement of the Hg
741 magnetometer. Although these do not necessarily have a direct impact upon
742 the EDM measurement, we summarize them here for completeness.

743 First, an analog of the Bloch-Siegert-Ramsey shift is the light shift due to
744 virtual transitions caused by the probe light beam. The size of this effect is
745 estimated to be 0.15 ppm, both by calculations from first principles and as
746 assessed in the data by looking for frequency versus light intensity correlations:
747 the latter analysis was used, as described above, to correct for this shift.

748 Next, there is a real transition shift caused by the fact that about 10 % of
749 the Hg atoms used to measure the final phase have been excited once before.
750 In the excited state they precess backwards through about 1° , and some of
751 the polarization survives the excitation and decay. The effect is as though
752 the gyromagnetic factor and precession frequency were reduced by 0.1 ppm in
753 the auxiliary trap and by 0.25 ppm in the data-taking trap. These shifts are
754 expected to be completely unchanged by the reversal of B_0 .

755 The total Hg absorption of the light beam is typically 15%, which gives us
756 a nearly optimum signal-to-noise ratio. Each atom that absorbs a photon is
757 depolarized after the subsequent spontaneous decay ($\tau = 1.2 \times 10^{-7}$ s). The
758 ensemble spin depolarization rate from this cause is about 1/1800 s. The typ-
759 ical observed total spin depolarization rate is 1/60 s. The contribution from
760 magnetic-field inhomogeneity is expected to be about a hundred times less than
761 that of the neutrons (1/600s) making it a negligible 1/60000 s. The dominant
762 relaxation rate, close to 1/60 s, is due to spin relaxation when the Hg atoms
763 stick on the wall.

764 The Hg initial phase is established by the two-second 90° spin-flip using a
765 rotating field at 8 Hz. Each Hg atom makes about 2000 free paths in the trap

766 during the spin-flip, so the phase information is very uniformly implanted over
 767 the trap volume. It continues to become more and more uniformly spread by the
 768 Hg motion while the neutrons are flipped using rf at 30 Hz. The initial Hg phase
 769 is then sampled on the basis of the 1% of Hg atoms that absorb a photon from
 770 the light beam during the next 15 s. (These atoms are partly depolarized in
 771 the process.) The final Hg phase is determined from the Hg atoms that absorb
 772 a photon in the last 15 seconds before the second UCN spin flip. There are a
 773 number of reasons why the Hg frequency, thus determined, does not represent
 774 a perfect volume average of the field:

- 775 1. Finite volume of the light beam: For all the Hg atoms that absorb a
 776 photon to measure the final phase, the last 1 millisecond of trajectory
 777 must certainly be near the light beam. This creates a phase bias. The
 778 B_0 field near the light could be different by 10^{-3} fractional compared
 779 with the volume average. This is 0.01 ppm of the total phase previously
 780 accumulated. The bias should be the same both for the initial and final
 781 phase measurements, so that it cancels out. The overall shift is expected
 782 to be less than 0.001 ppm.
- 783 2. Artefacts: The system of determining the frequency in the light detector
 784 signal has been tested at the 0.1 ppm level by feeding in sine waves from
 785 the frequency synthesiser.
- 786 3. Bias from Hg atoms dwelling on the wall: Free path transits take about
 787 10^{-3} s. The sticking time on the wall is thought to be about 10^{-8} s. Thus,
 788 the overall average has a surface average weighting of 10^{-5} compared to
 789 the volume average. The surface average value of B_z may differ by one
 790 part per thousand from the volume average, causing an overall error of
 791 about 0.01 ppm.
- 792 4. Bias due to surface relaxation or differential loss: This may occur if the
 793 relaxation is faster on one wall than another, or if there is a loss of atoms
 794 preferentially at one end of the cell. Suppose, for example, that the roof
 795 has an excess relaxation rate of 1/100 s compared with the other surfaces.

Each atom is colliding at about 1000 Hz, of which 250 Hz is on the roof. The probability of depolarization per roof collision is thus $P = 4 \times 10^{-5}$. We have analysed this problem and find that a shift occurs in the centre of measurement. Under the most pessimistic assumptions the shift Δh can reach the value $(H/8)P$, where H is the trap height – in this case, $(5 \times 10^{-6})H$, or 6×10^{-4} mm. When the magnetic field is not trimmed, the maximum $\partial B_z/\partial z$ gradients are 10^{-5} fractional per mm, or 1 nT/10 cm. The systematic bias from Δh is thus 0.006 ppm.

5. False EDM due to surface relaxation: The temporary increase in relaxation observed each time the HV polarity is reversed has been discussed above. This process swings some of the depolarisation rate backwards and forwards from roof to floor in synchronism with the HV polarity change. This can create a false EDM signal via a finite $\partial B_z/\partial z$. The transient partial relaxation rate averaged over an HT dwell is observed to be about 1/100 s, making a displacement of 6×10^{-4} mm. In the case of a $\partial B_z/\partial z$ gradient of 0.35 ppm/mm (corresponding to an R_a shift of 1 ppm), the systematic false field change seen by the Hg magnetometer is about 2×10^{-4} ppm or 2×10^{-16} T. This corresponds to a false EDM of about 2×10^{-27} e cm, some 1/20th of the geometric-phase false EDM. In practice it would have the same signature as the geometric phase false EDM, being proportional to R_a and changing sign with the direction of B_0 . It would simply act to increase the gradient of both data lines by about 5%. Currently the lines have a fitted gradient that is 20% \pm 15% above the GP phase theoretical prediction. This additional effect could easily be present. All of its consequences have been covered by our GP corrections.
6. Finally, variation of light intensity with HV has been dealt with above. If there were preferential depolarization of Hg on, say, the positive electrode, thus biasing the volume-averaged frequency measurement, it could slightly alter the gradients of the lines in Fig. 2 of [1], similarly to other gradient-changing mechanisms listed; but again, it is not a cause for concern as it does not affect the outcome of the analysis.

827 5.3. *The magnetic field*

828 To carry out a magnetic resonance experiment one must impose conditions
829 on both the homogeneity and the time stability of the magnetic field: the field
830 must be sufficiently homogeneous to retain polarization of the neutrons until the
831 end of the storage time, and it should be sufficiently stable so as not to increase
832 significantly the uncertainty in the determination of the precession frequency
833 beyond that due to neutron counting statistics.

834 5.3.1. *The magnetic shield*

835 In the environment of the experimental area magnetic field changes of up to
836 $1\text{ }\mu\text{T}$ in a few tens of seconds are quite common, and are often associated with
837 movements of the reactor crane, or with the operation of magnetic spectrometers.
838 To provide the required homogeneity and stability of the magnetic field,
839 the neutron storage volume was set inside a four-layer μ -metal magnetic shield.
840 The dimensions of the magnetic shield layers are given in Table I. The two inner
841 layers and their detachable endcaps had welded joints, and were annealed in a
842 reducing hydrazine (N_2H_4) atmosphere at $1050\text{ }^\circ\text{C}$ after manufacture [81]. The
843 two outer layers, which were too large to have been fired in a single piece, were
844 made from sheets of μ -metal individually annealed and bolted together with
845 150 mm overlaps. All four layers had 210 mm diameter holes at the top and
846 bottom of the mid-plane of the central cylinder: The bottom hole contained the
847 neutron guide tube, and the top contained the high-voltage feedthrough. The
848 endcaps of the innermost layer had a 45 mm hole in the center, and each of the
849 other three layers had a 32 mm hole. Originally, the apparatus had been built
850 with a fifth, innermost, layer of shielding, which was removed in the meantime
851 to allow for enlargement of the storage vessel. The shielding factor for the set of
852 five shields was measured by winding a pair of coils around the external shield
853 frame and measuring the magnetic field change at the center of the shields with
854 three rubidium magnetometers. The dynamic shielding factor to external mag-
855 netic field changes was found to be approximately 2×10^5 radially and 2×10^4
856 axially [82]. With the four-layer shield, the shielding factor transverse to the

Shield	R (m)	l_1 (m)	l_2 (m)	Overlap (m)	t (mm)
1	0.97	2.74	2.74	0.20	1.5
2	0.79	2.30	2.30	0.20	1.5
3	0.68	0.75	1.89	0.12	2.0
4	0.58	0.75	1.63	0.12	2.0

Table 1: The dimensions of the four-layer magnetic shield. Each layer consisted of a central cylinder, of radius R and length l_1 , and two detachable endcaps. The length l_2 is that of the central cylinder plus the endcaps, when assembled. The overlap is the distance by which the endcaps overlapped the central cylinders. t is the thickness of the μ -metal used in both the central cylinders and the endcaps.

axis is approximately 1.5×10^4 , consistent with expectation and also with comparisons made between changing external fields and changes registered by the mercury magnetometer.

5.3.2. The magnetic field coil

The coil to generate the $1 \mu\text{T}$ static magnetic field \mathbf{B}_0 was wound and glued directly onto the aluminum vacuum vessel. The coil fitted snugly inside the innermost layer of the magnetic shield and was wound with a $\cos\theta$ distribution to give a constant number of turns per unit distance along the vertical diameter of the cylinder. Theoretically a coil of constant pitch wound on the surface of a cavity inside a material of infinite permeability produces a homogeneous magnetic field, regardless of variation in the cross-sectional area of the cavity. The coil winding used here was an approximation to this ideal state. The turns were wound 20 mm apart, and access to the neutron trap required breaking all of the turns in order to remove the end of the cylinder. Every turn on the coil, therefore, had two breaks on each end face of the cylinder, where the electrical connection was made with a brass screw and two brass solder tags. The magnetic field was aligned with the vertical diameter of the cylindrical shield, rather than along the axis, to take advantage of the fact that the radial magnetic shielding factor is greater than the axial shielding factor.

The choice for the magnitude of \mathbf{B}_0 was arbitrary, in the sense that it does

not enter directly into the expression for the sensitivity of the experiment. There are, however, a number of other factors that had a strong bearing on the choice, *viz*: the field should be large compared to any residual fields inside the trap (≤ 2 nT), so that the axis of quantization for the neutrons, which is determined by \mathbf{B}_0 , is in the same direction everywhere; the field should be large enough to prevent depolarization of the neutrons as they pass into the shields; the homogeneity requirements given below must be fulfilled (in general, field gradients increase linearly with the field itself, thus placing a limit on the maximum field); the field should be as stable as possible, which is generally easier to achieve at lower fields; and finally, it was desirable to keep the precession frequency away from the 50 Hz mains frequency. The 1 μ T magnetic field chosen in this case gave a resonant frequency of about 30 Hz for the neutrons.

The coil that generated the \mathbf{B}_0 field had a resistance of approximately 10 Ω , and required a current of 17 mA to provide the 1 μ T field. The stabilizer providing this current contained a precision voltage reference with a very low output voltage temperature coefficient (National Semiconductors LM169B; 1 ppm/ $^{\circ}$ C) and an operational amplifier with a very low input offset voltage temperature coefficient (Analog Devices OP177A; 0.03 μ V/ $^{\circ}$ C). High-stability precision wirewound resistors (3 ppm/ $^{\circ}$ C) were used to define the \mathbf{B}_0 field current. High thermal conductivity resin was used to connect the components to the inside of a cylindrical aluminum block (approximately 100 mm in diameter and 100 mm long). This block, which acted as a heat reservoir for the temperature-critical components, was thermally isolated from the surroundings and from the power supply by more than 100 mm of polystyrene foam. The average electrical potential of the coil was maintained at the same potential as the vacuum tank upon which it was wound, in order to minimize currents to the coil supports.

5.3.3. Homogeneity

The homogeneity requirement for a magnetic resonance experiment in a low-field region is given by Ramsey [83], following the theory of the hydrogen maser [84]. Consider the neutron storage volume to be characterized by a length l and

to consist of two regions of magnetic field that differ by ΔB . If $\gamma = -2\mu_n/\hbar$ is the gyromagnetic ratio, then neutrons with velocity v passing from one field region to the other experience a relative phase shift of

$$\delta\phi = \gamma\Delta B l/v. \quad (26)$$

In a storage time T_s , the neutron will experience $M = vT_s/l$ such phase shifts, which will add randomly, so that the phase spread during the storage time is

$$\Delta\phi \approx \delta\phi\sqrt{M} = \gamma\Delta B\sqrt{lT_s}/v. \quad (27)$$

At the end of the storage time $\Delta\phi$ represents the typical phase difference between any two neutrons arising from them having followed different paths across the trap. Maintaining polarization requires that $\Delta\phi < 1$, from which arises the homogeneity constraint

$$\Delta B_0 < \frac{1}{\gamma}\sqrt{\frac{v}{lT_s}}. \quad (28)$$

904 It should be noted that it is the absolute inhomogeneity of the field ΔB_0 that
 905 is constrained, and not the relative homogeneity $\Delta B_0/B_0$. Taking $v = 5 \text{ ms}^{-1}$,
 906 $l = 150 \text{ mm}$, $T_s = 150 \text{ s}$ and $\gamma = 1.8 \times 10^8 \text{ radians s}^{-1} \text{ T}^{-1}$, the limit becomes
 907 $\Delta B_0 < 3 \text{ nT}$. For a B_0 field of $1 \text{ } \mu\text{T}$ this requires a relative homogeneity of
 908 $\Delta B_0/B_0 < 3 \times 10^{-3}$ over the 20-liter neutron storage volume.

909 The magnetic field within the storage volume was mapped using a three-
 910 axis fluxgate magnetometer probe [85]. As shown in Fig. 17, the field was
 911 found to be slightly quadrupolar in shape; the spatial variations were of the
 912 order of the $\approx 1 \text{ nT}$ resolution of the instrument, as long as the shield was
 913 demagnetized each time that the magnetic field configuration changed (i.e.,
 914 each time the magnetic shield was opened or the direction of \mathbf{B}_0 was reversed).
 915 Demagnetization was carried out by using a current loop that was threaded
 916 through all of the shields, parallel to the cylinder axis. The current was initially
 917 set to 100 ampère-turns, reversed every 2 s and steadily reduced to zero over
 918 twenty minutes. Trim coils were used to achieve this level of homogeneity;
 919 without them, the field variations would have been about four times greater.
 920 The T_2 neutron polarization relaxation time was typically about 600 s; the field

inside the trap was therefore adequately homogeneous to meet the requirements of the experiment.

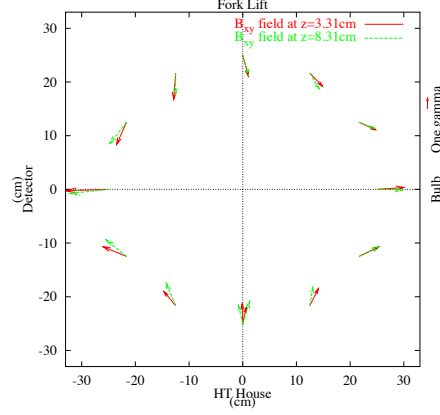


Figure 17: Scan of the magnetic field within the neutron storage volume, at two separate heights above the baseplate. The quadrupolar nature of the field is clear. The reference arrow on the right, marked “One gamma”, has a length corresponding to 1 nT. The labels “Fork Lift”, “Bulb”, “HT House”, “Detector” are direction indicators relating to surrounding apparatus: the shield axis runs from top to bottom on this plot. The figure is reproduced from the thesis of J.D. Richardson. [86]

5.3.4. Stability

In order to ensure that any noise on the EDM signal caused by magnetic field instabilities was significantly less than that due to neutron counting statistics, it was required that the shift in precession frequency between consecutive measurements should normally be not much larger than the uncertainty due to neutron counting statistics. Thus,

$$\left| \frac{dB_0}{dt} \right| \frac{\gamma T_s}{2\pi} \lesssim \frac{1}{2\pi\alpha T_s \sqrt{N}}. \quad (29)$$

For $\alpha = 0.5$, $T_s = 130$ s, and $N = 10\,000$ the constraint therefore becomes $|dB_0/dt| \lesssim 8$ fT/s. For $B_0 = 1$ μ T, this requires a stability of about one part per million over 130 s. However, this criterion is stricter than was necessary in this instance, for two reasons. First, the separated oscillating field method

928 itself is relatively insensitive to fluctuations in the magnetic field on time scales
 929 short compared with T_s . This is because the neutron counts are determined by
 930 the total accumulated phase difference between the neutron polarization and
 931 the oscillator, and not by a detailed comparison throughout the storage cycle.
 932 Second, the measured mercury precession frequency was used for normalisation.
 933 Except for a period of about 5% at either end of the storage time, any drifting of
 934 the magnetic field affected both spin systems in exactly the same manner, and
 935 averaging over the entire Ramsey measurement period reduced the influence of
 936 any changes that did occur during the end mismatch periods by an order of
 937 magnitude. In practice, though, condition (29) was usually satisfied. On the
 938 rare occasions when the field changed much more rapidly than this, the mercury
 939 precession was generally disturbed to such an extent that χ^2/ν for the frequency
 940 fit became extremely large, and the data point was rejected.

941 *5.3.5. Uncompensated magnetic field fluctuations*

942 In principle it is possible to have residual effects from \mathbf{B} field fluctuations,
 943 such as hysteresis in the μ -metal shield following disturbances in the stabilised
 944 \mathbf{B}_0 coil current supply caused by pickup from the high voltage changes. This
 945 would manifest itself most strongly as a dipole-like field \mathbf{B}_d originating from
 946 the μ -metal in the region of the HV feedthrough, which would be sensed by
 947 both the neutrons and the mercury magnetometer but with a difference given
 948 by $\delta B_d/B_d = 3\Delta h/r$ where $r \sim 55$ cm is the distance from the source of the
 949 field to the center of the trap. Thus, fluctuations in \mathbf{B} that are correlated with
 950 the HV can be expected to be compensated up to a factor of about 70. In order
 951 to study this, the mercury and neutron channels were analysed independently.

952 The analysis was performed by selecting sequences of measurement cycles
 953 within each run for which the magnetic field (as measured by the mercury
 954 frequency) varied smoothly throughout several high-voltage dwell periods. Both
 955 the mercury and the neutron frequencies for each such sequence were fitted to a
 956 low-order polynomial. The fits were unweighted, since the displacement from the
 957 fitted function was entirely dominated by the magnetic fluctuations rather than

958 by the uncertainties in the frequency calculation associated with each point.
 959 The residuals were then fitted to a linear function of the applied electric field to
 960 yield the apparent EDM measurements. A plot of the neutron vs. the Hg results
 961 (Fig. 18) shows complete (within uncertainties) correlation between the results,
 962 with the slope of the best-fit line (-3.83 ± 0.08) corresponding as expected to
 963 the ratio of gyromagnetic ratios.

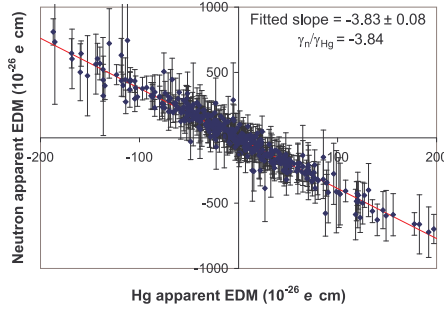


Figure 18: Apparent neutron EDM signals (due to uncompensated random magnetic field fluctuations) as a function of the corresponding apparent mercury EDM signals.

964 The neutrons yielded a net uncompensated EDM signal of $(17 \pm 4) \times 10^{-26}$
 965 $e\text{ cm}$; the Hg (once geometric-phase-induced false EDM contributions[51] had
 966 been subtracted) yielded $(-3.9 \pm 0.8) \times 10^{-26} e\text{ cm}$. These results are consistent
 967 with a common source of magnetic fluctuations correlated with the HV. We
 968 therefore expect the mercury-magnetometer compensation to shield us from
 969 this systematic effect to a level of $17 \times 10^{-26}/70 = 2.4 \times 10^{-27} e\text{ cm}$.

970 5.4. The electric field

971 The main requirements for the electric field were that it should be as large
 972 as possible and aligned with the magnetic field, but with the constraint that the
 973 leakage current through the insulator of the neutron trap should not generally
 974 exceed a few nanoamps. This latter restriction arises because the magnetic
 975 fields produced by currents circulating around the trap would induce shifts in
 976 the precession frequency that were correlated with the electric field. Although

977 such frequency shifts would be compensated to the level of at least 90% by the
978 mercury magnetometer, any residual effect could result in a systematic error in
979 the EDM, as discussed below.

980 Sparks could also in principle generate a systematic effect if they changed
981 the magnetization of the shields and if they occurred preferentially for one po-
982 larity of the electric field. However, the mercury magnetometer would naturally
983 compensate for any such effect, just as with any other shifts in the magnetic
984 field.

985 Sparks were also undesirable because, as discussed in Section (5.2.9) above,
986 they caused the mercury atoms to depolarize rapidly. The frequency at which
987 sparks occurred depended upon the voltage used, the quality of the vacuum,
988 and the conditioning of the system [73]. Sparks occurred more frequently when
989 the experiment was under vacuum ($\approx 10^{-6}$ torr) than they did when a pressure
990 of 10^{-3} torr of either dry nitrogen or helium was maintained in the system.
991 Helium was found to be more efficient than nitrogen in quenching sparks.

992 Before the start of each data run, the electric field was raised as far as pos-
993 sible (typically 1.5 MV m^{-1}), maintained for several minutes, and then lowered
994 and applied with the opposite polarity. This was repeated several times. The
995 effect was to reduce both the quiescent current across the trap and to suppress
996 almost entirely the occurrence of sparks during normal data taking. It was then
997 necessary to “clean” the trap with a short high-voltage discharge in 1 torr of
998 O_2 (with a current of $130 \mu\text{A}$ for approximately two minutes at each polarity,
999 twice) in order to restore the depolarization time of the mercury to a reason-
1000 able value. To some extent the cleaning reverses the beneficial effects of the
1001 training, and so the cleaning period is kept as brief as possible. The maximum
1002 electric field used for data taking was 1 MV m^{-1} , since occasional high-voltage
1003 breakdowns tended to occur beyond this limit, resulting in a reduction in the
1004 mercury depolarization time.

1005 As sparks invariably disrupt the mercury frequency measurement, batch
1006 cycles that contain them are excluded from the analysis, so beyond the residual
1007 effects just discussed the sparks themselves cannot contribute to any artificial

EDM signals.

5.4.1. The high-voltage stack

The electric field was generated by a reversible Cockcroft-Walton type high voltage stack, shown schematically in Fig. 19. The stack was powered by a controller from Bonar Wallis [87].

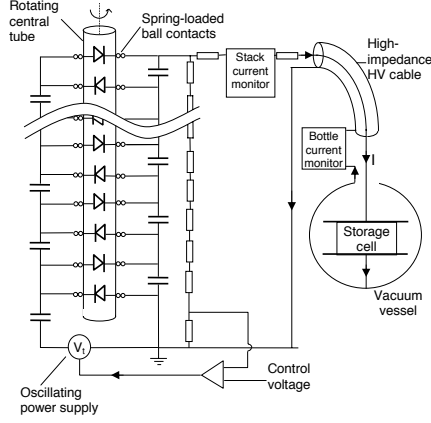


Figure 19: The reversible Cockcroft-Walton type high-voltage stack, and the current path through the EDM apparatus.

The polarity of the electric field within the neutron trap was reversed by changing the sign of the voltage applied to the ungrounded electrode. This was done by physically reversing the diodes in the charging stack, with the stack at zero voltage. The reversal was driven, under computer control, by a 180° rotation of the core of the stack using compressed air. The stack was connected to the neutron trap by 5 m of coaxial high-voltage cable with its central conductor removed and replaced with oil. A semiconducting sheath around the central conductor remained, and this provided the primary conducting path through the cable. There was a $1 \text{ G}\Omega$ resistance in series between the cable and the trap, to limit the current.

The stack, which was capable of providing $\pm 300 \text{ kV}$, was driven by a 20 kHz oscillator connected to the lowest of its 15 stages. Each stage was separated

1025 from its neighbors by a 3.6 nF capacitor, and a return current through a 2.8 G Ω
1026 resistor chain from the top stage was used by the controller to stabilise the
1027 output voltage.

1028 *5.4.2. Monitoring the high voltage*

1029 The electric field in the trap was monitored by recording the magnitude and
1030 sign of the voltage at the top of the stack, the current flowing through the stack,
1031 and the current in the feedthrough just above the trap, which charged up the
1032 electrodes (primarily displacement current) as the electric field was changed.
1033 Fig. 19 shows schematically how the current through the neutron trap was
1034 monitored. The coaxial arrangement of the trap and the return current path
1035 ensured that the magnetic effects of this current were minimized. This design
1036 arose from the experience gained in the earliest version of this experiment: At
1037 that time, the vacuum vessel was a glass jar, and no coaxial return current
1038 path was available. Sparks within the experimental apparatus were then seen
1039 to magnetize the shields permanently, producing changes of as much as 1 mHz
1040 in the precession frequency of the neutrons. With the arrangement described
1041 here no such effects were seen in this experiment.

1042 *5.4.3. Leakage currents and their effects*

1043 By a suitable choice of the high-voltage setting the quiescent current through
1044 the trap was typically kept at or below a few nA. The distribution for both
1045 polarities is shown in Fig. 20.

If the current flows in an axial direction through (or along the surface of)
the insulator between the electrodes, the magnetic field that it produces will
be at right angles to \vec{B}_0 . This field will be small compared with \vec{B}_0 and will
produce a shift in the precession frequency that is independent of the polarity of
the electric field; thus, this will not be a source of error in the measurement of
the EDM. However, one cannot assume that the current will take such a direct
path. The insulator is likely to contain paths of different resistances, which
could lead to the current having a net azimuthal component. (The insulator

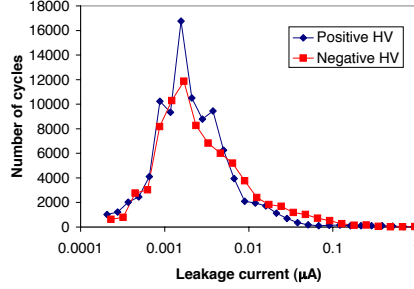


Figure 20: Distribution of the average leakage currents observed during each batch cycle. I

ring showed some mild discoloration indicating the path of discharges along its surface. For the most part these were vertical, but occasionally they were at an angle of up to 45° . It is likely that discharges along the surface of the insulator occurred most often in the vicinity of the windows for the mercury light.) In this case, a component of the magnetic field due to the current would be parallel (or anti-parallel) to \vec{B}_0 and would produce a frequency shift that changes sign when the polarity of the electric field is reversed, giving rise to a systematic error in the EDM. This effect can be estimated for the case in which the current I makes a fraction f of a complete turn around the insulator. If the insulator has radius r , the magnetic field at the center of this current loop is

$$B = \frac{\mu_0 I}{2r} \cdot f. \quad (30)$$

The mercury should compensate for the resulting frequency shift at a level of 90% or more. The current would therefore generate an artificial EDM signal of magnitude

$$|d| = 0.1 \frac{\mu_n}{E} \frac{\mu_0 I}{2r} \cdot f. \quad (31)$$

1046 As shown above, leakage currents are normally of the order of 1 nA. If the current
 1047 travels an azimuthal distance of 10 cm around the 47 cm diameter trap, the
 1048 applied electric field of $E = 1$ MV/m would give a false signal of order 0.1×10^{-27}
 1049 e cm. Fig. 21 shows the binned weighted-average frequency shifts (i.e., the
 1050 departures from the fitted Ramsey curves of the individual measurement cycles)

1051 as a function of the leakage current. The frequency shifts are multiplied by the
 1052 product of the polarities of the electric and magnetic fields. No dependence on
 1053 leakage current is apparent.

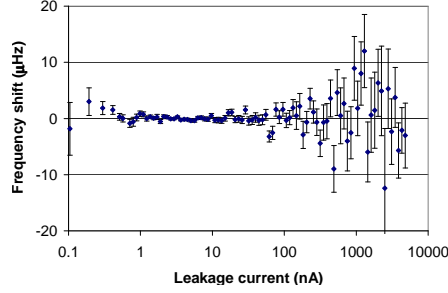


Figure 21: Frequency shifts (multiplied by the polarities of the electric and magnetic fields) as a function of leakage current.

1054 The displacement current as the voltage is ramped up and down was typically
 1055 $1 \mu\text{A}$. The magnitude of this, along with the known capacitance of the trap,
 1056 provided the necessary evidence that the applied voltage was reaching the trap.
 1057 The current flowing through the trap was not measured directly. The measured
 1058 current included currents flowing in the high-voltage feedthrough and cable
 1059 assembly, and it therefore should be regarded as an upper limit for the current
 1060 that flowed through the trap.

1061 5.5. HV AC ripple

1062 Changes in precession frequency may be caused by oscillating magnetic fields
 1063 at non-resonant frequencies through Bloch-Siegert-Ramsey type effects [62]. An
 1064 example in this class is a “ripple” on the high voltage, which would generate
 1065 an oscillating displacement current in the storage chamber and thereby an os-
 1066 cillating B field. The ripple amplitude may change with the sign of the high
 1067 voltage, producing slightly different frequency shifts for each of the two high
 1068 voltage polarities.

Consider the presence of an oscillating field $\vec{B}_2 \sin \omega_2 t$ in addition to the static field \vec{B}_0 and the resonant alternating field \vec{B}_1 . During the storage time

T_s , when \vec{B}_1 is off, the magnetic field in the trap is

$$\vec{B}_t = B_0 \hat{k} + B_2 \sin \omega_2 t \hat{i}. \quad (32)$$

For $B_2 \ll B_0$ and $\omega_2 \gg T_s^{-1}$, the time-averaged magnitude of this field is

$$\langle B_t \rangle \approx B_0 \left(1 + \left(\frac{B_2}{2B_0} \right)^2 \right). \quad (33)$$

The precession frequency therefore becomes

$$\nu'_0 = \nu_0 \left(1 + \left(\frac{B_2}{2B_0} \right)^2 \right), \quad (34)$$

1069 where ν_0 is the frequency in the absence of \vec{B}_2 .

The most probable source of an AC magnetic field is the 20 kHz oscillator that drives the high-voltage stack. This current keeps the capacitors charged against the losses due to the monitoring current. If the driving frequency is ω_2 and the monitoring current is I_s , the voltage associated with this current is

$$\mathcal{E} = \frac{I_s}{\omega_2 C}, \quad (35)$$

1070 where C is the capacitance of the stack. For the fifteen-stage stack with one
1071 3.6 nF capacitor per stage, $\omega_2 = 1.3 \times 10^5$ rad/s and $I_s = 100 \mu\text{A}$, equation (35)
1072 yields $\mathcal{E} = 3$ V.

1073 The capacitance of the trap, as calculated for a pair of parallel plates, is
1074 15 pF, which, at 20 kHz, has an impedance of 0.5 M Ω . This shorts out the DC
1075 resistance of the trap. Between the stack and the trap is a 1 G Ω resistor chain,
1076 so that 3 V produces a 3 nA alternating current. This current flows through
1077 the trap as a displacement current and produces an AC magnetic field whose
1078 magnitude, averaged over the volume of the trap, is of the order of 1 fT. This
1079 would give a frequency shift of $\approx 10^{-17}$ Hz and a systematic error in the EDM
1080 at the level of $\approx 10^{-36}$ e cm, which is a completely negligible effect.

1081 AC fields at mains frequency are another possible cause of concern. There
1082 is no differential ripple visible on the HV at the level of a few volts. Sampling
1083 is done at 5 Hz with a bandwidth of 20 kHz, so any 50 Hz ripple would show

up as beats. This is certainly absent at the level of, say, 50 V, which would give a false EDM of 0.01×10^{-27} e cm.

Low-frequency AC fields were sought by means of a pickup coil in conjunction with a phase-sensitive detector. Shifts in R from this source at the level of 0.02 ppm could not be ruled out. Cancellations in the corresponding EDM signal from reversals of the electric and magnetic fields would reduce any net contribution to below the level of 0.01×10^{-27} e cm.

5.5.1. *Electric forces*

Another possible source of systematic error arises from electrostatic forces, which may move the electrodes slightly. In conjunction with a magnetic field gradient, an HV-dependent shift in the ratio would then appear. This was sought by looking for an EDM-like signal but with a frequency shift proportional to $|\mathbf{E}|$ instead of to \mathbf{E} . The $|\mathbf{E}|$ signal, at $(-2.4 \pm 3.8) \times 10^{-26}$ e cm, was consistent with zero. If the HV magnitudes were slightly different for the two signs of \mathbf{E} , this effect would generate a false EDM signal. Study of the measured HV and of the charging currents show that the HV magnitude was the same for both polarities to within an uncertainty of about 1%. This systematic uncertainty is therefore 1% of the $|\mathbf{E}|$ uncertainty, i.e. 0.4×10^{-27} e cm.

6. The data-acquisition process

A data-taking run lasted for up two days and involved a sequence of operations built around the continuous repetition of the basic Ramsey measurement cycle outlined in Section 4. This cycle lasted for approximately four minutes, and involved filling the trap with polarized neutrons and mercury, applying the separated oscillating fields sequence, releasing and counting the neutrons in the original spin state, and finally releasing and counting the neutrons in the other spin state. Each cycle gave rise to a single neutron frequency measurement. Approximately once per hour, the direction of the electric field was reversed. The operation was controlled by a PC running LabVIEW-based software.[88]

1112 6.1. *Filling*

1113 The trap was filled for 20 s, corresponding to approximately 1.3 filling time
1114 constants, after which the density of UCN was about 2 cm^{-3} . The polarization
1115 at this time was approximately 75%. The stored neutrons had their spins aligned
1116 antiparallel to the magnetic field in the trap (denominated “spin up”). At this
1117 point the neutron door was closed, and the door from the mercury prepolarizing
1118 cell was opened for 1 s, allowing the polarized mercury atoms to enter.

1119 6.2. *Ramsey sequence*

1120 The Ramsey sequence then began, with a 2 s interval of rotating magnetic
1121 field \mathbf{B}'_1 (in the horizontal, or xy , plane) to allow the mercury polarization to
1122 precess down into the xy plane, followed by a 2 s interval of (horizontal) oscillat-
1123 ing field \vec{B}_1 to turn the neutron polarization in similar fashion. The \mathbf{B}_1 field was
1124 aligned with the cylinder axis of the shield and it was generated by a Helmholtz
1125 pair of current-carrying wire turns on the vacuum vessel. The current was pro-
1126 vided by an HP 3325B frequency synthesiser[89]. The inner magnetic shield
1127 acted as a return for the flux. The \mathbf{B}'_1 field (for the mercury) was a superpo-
1128 sition of two perpendicular linear oscillating fields, 90° out of phase, generated
1129 in an identical manner by their own Helmholtz pairs. The simple nature of the
1130 coils, and the distorting effects of eddy currents in the vacuum chamber wall
1131 and other metal parts, caused the oscillating field to vary in strength by about
1132 10% over the volume of the neutron trap. Conveniently, the rapid motion of the
1133 mercury and neutrons inside the trap provided sufficient averaging in the 2 s
1134 duration chosen for each r.f. pulse interval that, in spite of this inhomogeneity,
1135 there was a negligible loss of polarization while turning the polarization vectors
1136 into the xy plane. The fact that the neutrons remained relatively undisturbed
1137 during the four-second period after the closing of the neutron door and before
1138 the \mathbf{B}_1 pulse was applied allowed the neutron velocity distribution to relax to-
1139 wards isotropy, and the spatial distribution to relax towards uniformity. This
1140 should have minimized any systematic $\mathbf{v} \times \mathbf{E}$ effect arising from the Lorentz
1141 transformation of the electric field into the neutrons’ rest frame.

1142 A 130 s interval T_{fp} followed in which the spin polarizations precessed freely
 1143 in the xy plane about the \mathbf{B}_0 and \mathbf{E} fields. The choice of the length of T_{fp}
 1144 depended upon several factors: (i) the storage lifetime of neutrons in the trap
 1145 (about 200 s); (ii) the T_2 relaxation time of the neutrons (about 600 s, although
 1146 times as long as 1000 s were seen under the best conditions); (iii) the result-
 1147 ing width of the resonance; (iv) the dead time spent in filling and emptying the
 1148 trap, since the sensitive period T_{fp} should be as long as possible in comparison to
 1149 them; (v) the signal-to-noise and the depolarization time of the mercury, which
 1150 affect the accuracy of the frequency measurement; and (vi) the needs of other
 1151 users of the TGV neutron source, whose measurement cycles had to be inter-
 1152 leaved with those of the EDM experiment. The maximum statistical sensitivity
 1153 was achieved by maximizing, as far as possible, the quantity $\alpha E T_{fp} \sqrt{N_b / T_{\text{tot}}}$,
 1154 where T_{tot} is the total time taken for the measurement cycle and N_b is the
 1155 number of neutrons per batch cycle. This function is, in fact, rather flat in the
 1156 region of the 130 s storage time that was used.

1157 6.3. Counting

1158 The free precession was brought to an end when the frequency synthesiser
 1159 was gated on to the coil to provide the second 2 s interval of the oscillating B_1
 1160 field. Immediately afterwards, the door of the trap was opened. The polariz-
 1161 ing foil then served as an analyzer and let through to the detector only those
 1162 neutrons that project into their original spin-up state. After 8 s of counting,
 1163 a fast-adiabatic-passage spin-flip coil, adjacent to the polarizer, was energized.
 1164 The spin-down neutrons, which had until this time been unable to pass the
 1165 polarizer, then received a 180° spin flip whenever they traversed the spin-flip
 1166 coil. This permitted them to pass through the polarizer and on to the detector.
 1167 They were counted in a separate scaler for 20 s, before the system reverted
 1168 to continued counting of the spin-up neutrons for a final 12 s. Counting the
 1169 spin-down neutrons served a triple purpose: it increased the sensitivity of the
 1170 experiment by increasing the number of neutrons counted; it emptied the trap
 1171 of neutrons that would be in the “unwanted” spin state when refilling at the

beginning of the next cycle; and finally, it provided a way of eliminating noise that would be introduced by fluctuations, additional to those of normal counting statistics, in the initial number of stored neutrons after filling. The spin-up and spin-down counts belong to different Ramsey resonance patterns that are 180° out of phase. Splitting the spin-up counting into two periods and inserting the spin-down counting in between them allowed us approximately to equalise the efficiency of detection of the UCN leaving the trap in each state.

The first batch of any run is different from any of the others, as the neutron trap and guides are initially empty; for other batches there is likely to be some remnant population from the previous batch. In consequence the first batch often had an anomalously low total neutron count (and would normally be excluded from analysis).

6.4. *Timing*

The timing of the various stages of the measurement cycle was controlled by a dedicated microprocessor. It was installed as a CAMAC unit so that at the start of a run the interval lengths to be used, and the corresponding states of the various valves and relays, could be loaded into the microprocessor memory from the PC that was in overall control of the data acquisition.

After it had started a cycle, the PC became completely passive with respect to timing. It received signals from the timer that told it the logical state of each hardware control. As each cycle neared its end, the PC awaited an end-of-sequence signal from the timer, at which point it immediately restarted the timer sequence for the next cycle. This ensured that the timing within the cycle, which could potentially influence the number of neutrons counted, could not be affected by the state of the high voltage in some unforeseen way through the action of the software. End-of-cycle tasks such as storing the data on disk and reprogramming the frequency synthesizer were carried out during the first few seconds of the subsequent cycle.

1200 6.5. High-voltage control

1201 The high voltage was controlled by a separate PC, and the associated con-
1202 trolling and monitoring electronics were kept entirely separate from the data-
1203 acquisition electronics. The PCs were networked via a common Ethernet hub.
1204 At the start of the run, and after each Ramsey measurement period, the data
1205 acquisition PC issued a request to set the appropriate voltage for the upcoming
1206 batch. The high-voltage PC transmitted in return a summary of measurements
1207 that it had made, such as the average voltage, leakage current, maximum cur-
1208 rent and so on, during the Ramsey measurement period that has just been
1209 completed. These data were stored along with all of the other information re-
1210 lating to that particular measurement cycle. Keeping the high voltage control
1211 separate from the data acquisition system minimised the possibility of some un-
1212 foreseen interaction that might result in a false EDM signal. The initial polarity
1213 of the high voltage at the start of the run was chosen randomly by the software.

1214 The high voltage changed with a pattern that repeated every 32-40 mea-
1215 surement cycles (collectively known as a “dwell”), the exact sequence being
1216 programmed as desired at the start of the run. There were typically 16 cycles
1217 with the electric field applied, say, parallel to the magnetic field, followed by two
1218 or four cycles at zero electric field, before the sequence was repeated with the
1219 electric field reversed. The electric field did not normally attain its full value
1220 until the second cycle of each dwell, because it took a significant amount of time
1221 to reverse the polarity and to ramp up the voltage. Only the 40 s period during
1222 which the neutrons were being counted was used to change the electric field; the
1223 voltage was frozen at the start of the measurement cycle, allowing it to settle
1224 and the leakage currents to fall during the neutron filling period so that it was
1225 stable during the sensitive Ramsey measurement period. Data taken during the
1226 first batch cycle of each high-voltage dwell are therefore valid, and are used in
1227 the analysis, but have a reduced sensitivity relative to the majority of other
1228 cycles because of their lower electric fields. In principle, it would have been
1229 possible to ramp up fast enough to complete the polarity change within one
1230 40 s period, but doing so would have increased both the displacement current

1231 and the probability of sparks occurring.

1232 Thus, the electric field is taken through a cycle of changes that has a repe-
1233 tition period of about 2 hours. The length of this period was chosen with the
1234 following considerations in view: The magnetic field had slow drift noise, or
1235 what might be called “ $1/f$ ” noise, which, if not treated properly, might have
1236 made a significant contribution to the statistical error on the measurement of the
1237 EDM. The use of the electric field reversal sequence with a period T_E makes it
1238 possible to reduce the noise contributions coming from the spectral components
1239 of the drift with period T_sp by a factor which is approximately T_sp/T_E . Thus,
1240 shortening the period for the electric field sequence increased the attenuation
1241 for the drift noise at very low frequencies and extended the attenuating effects
1242 to higher frequencies. Furthermore, the system was constrained by the behavior
1243 of the mercury; it was usually necessary to end a run after a day or two in order
1244 to discharge-clean the trap so as to restore the mercury depolarization time.
1245 Since it was clearly desirable to have several complete high-voltage dwell peri-
1246 ods within each run, one hour was a reasonable maximum time limit between
1247 polarity reversals. The disadvantage of shorter dwell sequences is that more
1248 time would have been spent at low voltages while the field was being ramped;
1249 and, in addition, the mercury depolarization time took an hour or so to recover
1250 from the dramatic fall that it suffered at each polarity reversal (see Fig. 15).

1251 Study of the measured HV and of the charging currents show that the HV
1252 magnitude was the same for both polarities to within an uncertainty of about
1253 1%.

1254 6.6. Neutron frequency tracking

The mercury frequency ν_{Hg} for each cycle was used to derive a first-order estimate

$$\nu'_0 = \nu_{Hg} \frac{\gamma_n}{\gamma_{Hg}} \quad (36)$$

for the neutron resonant frequency. This allowed the applied synthesizer frequency ν_1 to be adjusted on a cycle-by-cycle basis in order to track variations in

the magnetic field. The frequency ν_1 was made to differ from ν'_0 by an amount

$$\delta\nu = \nu'_0 - \nu_1 \quad (37)$$

where $\Delta\nu$ is the linewidth given by equation (13) and f was chosen sequentially to be -0.55, +0.45, -0.45, +0.55, so as to follow the pairs of working points on either side of the central fringe of the resonance as shown in Fig. 3.

6.7. Measurement and storage of data

The state of the experiment was monitored and recorded using 24-bit scalers and 12-bit, 10 V ADCs that were read at various points during each measurement cycle, as well as by the 16-bit ADC used to record the oscillating mercury signal. The values of about fifty parameters were written to disk for each cycle. These parameters included the neutron counts for each of the two spin states; neutron counts registered by the flux monitor on the input guide tube; the frequency of the applied oscillating \vec{B}_1 field; the fitted mercury frequency, amplitude and depolarization time, with their associated uncertainties; the high voltage magnitude and polarity; average and maximum leakage currents during the Ramsey measurement period; and various supplemental information, such as the temperature and humidity of the environment. The mercury ADC readings were stored in separate files, in case the need should arise to reanalyze and refit them. For each run, a multichannel analyzer (LeCroy[90] qVt module) recorded the pulse-height spectrum from the neutron detector, and this spectrum was also recorded on disk so that the performance of the detector could be monitored over time. In addition, values for the voltage and current in the HV system were digitised at a rate of 5 Hz, and these readings were also recorded separately so that the high-voltage performance of the system could be examined in detail for any given run.

A single run typically lasted for one to two days, and therefore incorporated about 300 batch cycles.

1280 7. Conclusion

1281 We have presented here a complete description of the apparatus used in
1282 the experimental measurement of the electric dipole moment of the neutron at
1283 ILL, Grenoble, and discussed many aspects of the hardware that could have
1284 introduced systematic errors into the results. The equipment was used to take
1285 data from 1996 until 2002, at which time it was decommissioned. At the time
1286 of writing, this experiment has provided the world’s most sensitive limit on the
1287 neutron EDM.

1288 Acknowledgments

1289 We acknowledge with gratitude the contributions of Prof. N.F. Ramsey, orig-
1290 inal pioneer of the entire series of neutron EDM experiments, for his invaluable
1291 interest and support throughout this long program of work. During the many
1292 years of research and development that lie behind this publication, there have
1293 been many significant individual contributions. Here, we would like to acknowl-
1294 edge the contributions made by Ph.D. students from the University of Sussex to
1295 the previous neutron EDM experiment, upon which the apparatus for this mea-
1296 surement was strongly based and in whose theses detailed prescriptions for many
1297 of the early experimental techniques can be found, namely A.R. Taylor (1977);
1298 T. Sumner (1979); S.M. Burnett (1982); P. Franks (1986); P.M.C. de Miranda
1299 (1987); N. Crampin (1989); and D.J. Richardson (1989). One of us (DJM)
1300 benefitted from an ILL studentship. Much of the detailed on-site work with
1301 neutrons at the ILL was carried out by several generations of Research Fellows
1302 and engineers, and in this regard we would particularly like to thank R. Golub,
1303 J. Morse, H. Prosper and D.T. Thompson. Prof. L. Hunter alerted us to the
1304 possibility of a geometric-phase-induced systematic effect caused by the “con-
1305 spiracy” between $\partial B_z/\partial z$ and the $\mathbf{v} \times \mathbf{E}$ effect. We would like to thank Prof. C.
1306 Cohen-Tannoudji for useful discussion relating to frequency shifts caused by the
1307 mercury reading light. Prof. A. Serebrov of PNPI assisted us greatly with the
1308 provision of high-quality neutron guides. Prof. Lobashev, also of PNPI, helped

1309 us to obtain our first quartz-walled neutron containment vessel, and Natasha
 1310 Ivanov helped us to obtain various optical components. The experiments would
 1311 not have been possible at all without the cooperation and provision of neutron
 1312 facilities by the ILL itself. This work has been funded by the U.K. Science
 1313 and Technology Facilities Council (STFC) and by its predecessor, the Particle
 1314 Physics and Astronomy Research Council (PPARC). Much of the early magne-
 1315 tometry work, in particular that carried out at the University of Washington,
 1316 was supported by NSF grant PHY-8711762.

1317 References

- 1318 [1] C. Baker, et al., Phys. Rev. Lett. 97 (2006) 131801.
- 1319 [2] N. Ramsey, Rep. Prog. Phys. 45 (1982) 95.
- 1320 [3] S. Barr, W. Marciano, in: C. Jarlskog (Ed.), CP Violation, World Scientific,
 1321 Singapore, 1989.
- 1322 [4] R. Sachs, The Physics of Time Reversal, University of Chicago Press, 1987.
- 1323 [5] C. Wu, et al., Experimental test of parity conservation in beta decay, Phys.
 1324 Rev. 105 (1957) 1413.
- 1325 [6] A. Angelopoulos, et al., Phys. Lett. B 44 (1998) 43.
- 1326 [7] A. Alavi-Harati, et al., Phys. Rev. Lett. 84 (2000) 408.
- 1327 [8] J. Adams, et al., Phys. Rev. Lett. 80 (1998) 4123.
- 1328 [9] G. Lüders, Kgl. Danske Videnskab. Selskab, Mat.-fys. Medd. 28.
- 1329 [10] J. Schwinger, Phys. Rev. 91 (1953) 720.
- 1330 [11] J. Schwinger, Phys. Rev. 94 (1953) 1366.
- 1331 [12] J. Christenson, J. Cronin, V. Fitch, R. Turlay, Phys. Rev. Lett. 13 (1964)
 1332 138.

- 1333 [13] B. Aubert, et al., Phys. Rev. Lett. 87 (2001) 091802.
- 1334 [14] K. Abe, et al., Phys. Rev. Lett. 87 (2001) 091802.
- 1335 [15] D. Kirkby, Y. Nir, Phys. Lett. B 592 (2004) 136.
- 1336 [16] A. Alavi-Harati, et al., Phys. Rev. Lett. 83 (1999) 22.
- 1337 [17] S. Barr, Int. J. Mod. Phys. A 8 (1993) 209.
- 1338 [18] C. Jarlskog (Ed.), CP Violation, World Scientific, Singapore, 1989.
- 1339 [19] J. Ellis, Nucl. Instr. Meth. A 284 (1989) 33–39.
- 1340 [20] X.-G. He, B. McKellar, S. Pakvasa, Int. J. Mod. Phys. A 4 (1989) 5011.
- 1341 [21] J. Smith, E. Purcell, N. Ramsey, Phys. Rev. 108 (1957) 120.
- 1342 [22] P. Miller, W. Dress, J. Baird, N. Ramsey, Phys. Rev. Lett. 19 (1967) 381.
- 1343 [23] C. Shull, R. Nathans, Phys. Rev. Lett. 19 (1967) 384.
- 1344 [24] W. Dress, J. Baird, P. Miller, N. Ramsey, Phys. Rev. 170 (1968) 1200.
- 1345 [25] V. Cohen, R. Nathans, H. Silsbee, et al., Phys. Rev. 177 (1969) 1942.
- 1346 [26] J. Baird, P. Miller, W. Dress, N. Ramsey, Phys. Rev. 179 (1969) 1285.
- 1347 [27] S. Apostolescu, D. Ionescu, M. Ionescu-Bujor, et al., Rev. Roumaine Phys.
1348 15 (1970) 3.
- 1349 [28] W. Dress, P. Miller, N. Ramsey, Phys. Rev. D 7 (1973) 3147.
- 1350 [29] W. Dress, P. Miller, J. Pendlebury, et al., Phys. Rev. D 15 (1977) 9.
- 1351 [30] I. Altarev, Y. Borisov, A. Brandin, et al., Nucl. Phys. A 341 (1980) 269.
- 1352 [31] I. Altarev, Y. Borisov, N. Borovikova, et al., Phys. Lett. B 102 (1981) 13.
- 1353 [32] J. Pendlebury, K. Smith, R. Golub, et al., Phys. Lett. B 136 (1984) 327.
- 1354 [33] I. Altarev, Y. Borisov, N. Borovikova, et al., JETP Lett. 44 (1986) 460.

1355 [34] K. Smith, N. Crampin, J. Pendlebury, et al., Phys. Lett. B 234 (1990) 191.

1356 [35] I. Altarev, Y. Borisov, N. Borikova, et al., Phys. Lett. B 276 (1992) 242.

1357 [36] I. Altarev, Y. Borisov, N. Borikova, et al., Phys. Atomic Nuclei 59 (1996)

1358 1152.

1359 [37] P. Harris, C. Baker, K. Green, et al., Phys. Rev. Lett. 82 (1999) 904.

1360 [38] W. Griffith, M. Swallows, et al., Phys. Rev. Lett. 102 (2009) 101601.

1361 [39] B. Regan, E. Commins, C. Smidt, D. DeMille, Phys. Rev. Lett. 88 (2002)

1362 071805.

1363 [40] J. Hudson, D. Kara, et al., Nature 473 (2011) 493.

1364 [41] A. Vutha, W. Campbell, et al., J. Phys. B 43 (2010) 074007.

1365 [42] M. Kozlov, D. DeMille, Phys. Rev. Lett. 89 (2002) 133001.

1366 [43] A. Petrov, A. Titov, et al., Phys. Rev. A 72 (2005) 022505.

1367 [44] O. Lebedev, K. Olive, M. Pospelov, A. Ritz, Phys. Rev. D 70 (2004) 016003.

1368 [45] S. Abel, O. Lebedev, Neutron-electron edm correlations in supersymmetry

1369 and prospects for edm searches, JHEP 0601 (2006) 133.

1370 [46] N. Ramsey, in: Proc. XIV Int. Conf. Atomic Physics, AIP, New York, 1994,

1371 p. 3.

1372 [47] I. Khriplovich, S. Lamoreaux, CP Violation without Strangeness, Springer,

1373 1996.

1374 [48] F. Shapiro, Sov. Phys. Usp. 11 (1968) 345.

1375 [49] R. Golub, J. Pendlebury, Contemp. Phys. 13 (1972) 519.

1376 [50] S. Lamoreaux, R. Golub, Phys. Rev. Lett. 98 (2007) 149101.

1377 [51] J. Pendlebury, et al., Phys. Rev. A 70 (2004) 032102.

1378 [52] R. Golub, J. Pendlebury, Rep. Prog. Phys. 42 (1979) 439.

1379 [53] Y. Zel'dovich, Sov. Phys. JETP 9 (1959) 1389.

1380 [54] A. Stoika, A. Strelkov, M. Hetzelt, Z. Phys. B 29 (1978) 349.

1381 [55] W. Lanford, R. Golub, Phys. Rev. Lett. 39 (1977) 1509.

1382 [56] Montedison Group, Montefluos, Foro Buonaparte 31, Milano, Italy.

1383 [57] J. Bates, Phys. Lett. A 88 (1982) 427.

1384 [58] H. Goldenberg, D. Kleppner, N. Ramsey, Phys. Rev. 123 (1961) 530.

1385 [59] N. Ramsey, Molecular Beams, Oxford University Press, 1956.

1386 [60] N. Ramsey, Rev. Mod. Phys. 62 (1990) 541.

1387 [61] D. May, Ph.D. thesis, University of Sussex (1999).

1388 [62] N. Ramsey, Phys. Rev. 100 (1955) 1191.

1389 [63] F. Bloch, A. Siegert, Phys. Rev. 57 (1940) 522.

1390 [64] C. Baker, et al., Phys. Rev. Lett. 98 (2007) 149102.

1391 [65] A. Steyerl, H. Nagel, F.-X. Schreiber, et al., Phys. Lett. A 116 (1986) 347.

1392 [66] A. Steyerl, S. S. Malik, Nucl. Instr. Meth. A 284 (1989) 200–207.

1393 [67] A. Taylor, Ph.D. thesis, University of Sussex (1977).

1394 [68] S. Al-Ayoubi, Ph.D. thesis, University of Sussex (2002).

1395 [69] P. Harris, J. Pendlebury, N. Devenish, <http://arxiv.org/abs/1306.1252>, ac-
1396 cepted for publication in Phys. Rev. D.

1397 [70] W. Mampe, J. Bugeat, Phys. Lett. A 78 (1980) 293.

1398 [71] R. Herdin, A. Steyerl, A. Taylor, et al., Nucl. Instr. Meth. 148 (1977) 353.

1399 [72] P. de Miranda, Ph.D. thesis, University of Sussex (1987).

1400 [73] L. Alston, High Voltage Technology, Oxford University Press, 1968.

1401 [74] M. van der Grinten, J. Pendlebury, D. Shiers, et al., Nucl. Instr. Meth. A
1402 423 (1999) 421.

1403 [75] K. Green, P. Harris, P. Iaydjiev, et al., Nucl. Instr. Meth. A 404 (1998)
1404 381.

1405 [76] H. Dehmelt, Phys. Rev. 105 (1957) 1487.

1406 [77] H. Dehmelt, Phys. Rev. 105 (1957) 105.

1407 [78] Y. Chibane, S. Lamoreaux, J. Pendlebury, K. Smith, Meas. Sci. Technol. 6
1408 (1995) 11671.

1409 [79] C. Cohen-Tannoudji, J. Dupont-Roc, Phys. Rev. A 5 (1972) 968.

1410 [80] A. Corney, Atomic and Laser Spectroscopy, Oxford University Press, 1968.

1411 [81] Magnetic Shields Ltd., Headcorn Rd., Staplehurst, Kent TN12 0DS, U.K.

1412 [82] T. Sumner, J. Pendlebury, K. Smith, J. Phys. D 20 (1987) 1095.

1413 [83] N. Ramsey, Acta Phys. Hung. 55 (1984) 117.

1414 [84] D. Keppner, H. Goldenberg, N. Ramsey, Phys. Rev. 126 (1962) 603.

1415 [85] Bartington Instruments Ltd., 10 Thorney Leys Business Park, Witney, Ox-
1416 ford, OX28 4GG England. <http://www.bartington.com/form.htm>.

1417 [86] J. Richardson, Ph.D. thesis, University of Sussex (2006).

1418 [87] Bonar Wallis Electronics Ltd., Worthing, U.K.

1419 [88] National Instruments corporation, 6504 Bridge Point Parkway, Austin, TX
1420 78730-5039, U.S.A.

1421 [89] Hewlett-Packard inc., Palo Alto, CA, U.S.A.

1422 [90] LeCroy Research Systems, 700 Chestnut Ridge Road, Chestnut Ridge, NY
1423 10977, U.S.A.